The $^{20}Ne(n,p)^{20}F$ Reaction at $E_n = 198$ MeV Using a New High Pressure Gas Target

by

Barry William Pointon

B.Sc. University of British Columbia, 1985

A THESIS SUBMITTED IN PARTIAL FULFILLMENT OF

THE REQUIREMENTS FOR THE DEGREE OF

MASTER OF SCIENCE

in the Department

of

PHYSICS

SIMON FRASER UNIVERSITY

October 1989

APPROVAL

NAME: Barry William Pointon

DEGREE: Master of Science

TITLE OF THESIS: The $^{20}Ne(n,p)^{20}F$ Reaction at $E_n = 198$ MeV Using a New High Pressure Gas Target.

EXAMINING COMMITTEE:

Chairman: Professor E.D. Crozier

Professor Otto F. Häusser
Senior Supervisor

Dr. K.P. Jackson
Research Scientist, TRIUMF

Professor D.Boal
Dept of Physics, SFU

Dr. B.K. Jennings
Examiner
Research Scientist, TRIUMF

Date Approved: October 5, 1989

PARTIAL COPYRIGHT LICENSE

I hereby grant to Simon Fraser University the right to lend my thesis, project or extended essay (the title of which is shown below) to users of the Simon Fraser University Library, and to make partial or single copies only for such users or in response to a request from the library of any other university, or other educational institution, on its own behalf or for one of its users. I further agree that permission for multiple copying of this work for scholarly purposes may be granted by me or the Dean of Graduate Studies. It is understood that copying or publication of this work for financial gain shall not be allowed without my written permission.

Title of Thesis/Project/Extended Essay

The $^{20}Ne(n,p)^{20}F$ Reaction at $E_n = 198$ MeV Using a New High Pressure Gas Target

Author: ___ _____
(signature)

Barry Pointon
(name)

Dec 7, 1989
(date)

ABSTRACT

Cross sections of the ^{20}Ne(n,p)^{20}F reaction at E_n = 198 MeV were measured at five angles at the TRIUMF charge exchange facility. This measurement was made possible by the development of a new segmented high pressure gas target. A multipole decomposition was done to extract the $\Delta L=0$, $\Delta L=1$ and $\Delta L\geq 2$ contributions to the spectra. The Gamow-Teller strength, $B(GT)$, which is directly proportional to the cross section of the $\Delta L=0$ contribution at $q=0$, was found for both individual states and the total spectrum. The extracted GT strength is compared with that predicted by recent large basis shell model calculations using both free nucleon and effective operators. The difference between the measured $B(GT)$ and that calculated with free nucleon operators ('quenching') has been the subject of much recent study in the *sd* shell and other mass regions. In the region E_x=0–7.5 MeV in ^{20}F there is no net quenching seen even though the calculations do not accurately reproduce the experimental strength distribution. These results are compared with recent (p,p') and (p,n) measurements. The resulting $B(GT)$ is also compared to the related magnetic dipole strength in ^{20}Ne , $B(M1)$, found from photon and electron scattering, to examine the importance of the spin-orbital interference in the M1 matrix element. This interference enhances the $B(M1)$ of the 11.2 MeV, 1^+, T=1 state in ^{20}Ne by a factor of five. The systematics of quenching may lead to direct evidence for meson exchange currents in nuclei once the systematics of the spin-orbital interference is determined across the full *sd* shell. This research is part of such a survey being undertaken at TRIUMF.

DEDICATION

I would like to dedicate this thesis to my father and mother without whose love and support it would not have been possible.

εις δοξαν θεου

...He utters in each grain the unmixed image of His energy. Each grain if it spoke would say 'I am at the center. For me all things were made'. Let no mouth open to gainsay it. Blessed be He.

–**C.S.Lewis**, "Perelandra"

...τα παντα δι' αυτου

και εις αυτον εκτισται

και αυτος εστιν προ παντων

και τα παντα εν αυτω συνεστηκεν

(Colossians 1:16,17)

ACKNOWLEDGEMENTS

I would like to thank the many people who helped me during my research work. I would first like to thank Prof. Otto Häusser for his support and direction for the two and a half years of my research. I would also like to thank Dr. Robert Henderson for all his help on the target and Dr. Mike Vetterli, and Dr. Ken Hicks, for their patient help and instruction on what it all means. I would also like to thank the rest of the MRS collaboration for their help and comments on the experiment and its analysis. Finally I would like to thank my supervisory committee and examiner.

Contents

List of Figures

List of Tables

Chapter 1

Introduction

At the very center of every atom, just where we expect to find simplicity, there is great complexity. The atomic nucleus has a very rich and intricate structure. Since the discovery of the nucleus in 1911, much work has gone into understanding its structure, but this has been hampered by two problems. The first is that there is no complete theoretical description of the force between the constituents of the nucleus, the nucleons. There is a large body of nucleon-nucleon (NN) scattering data, but no theoretical interaction can accurately and consistently reproduce it. The second problem is that the nucleus is a strongly interacting, quantum many-body system, and there are no mathematical techniques to deal with such a system exactly. Simplifying models have been made with varying degrees of success.

Since the late 1940's the nucleus has been treated in a way analogous to the atomic shell model. Each of the nucleons is assumed to move independently in a specific orbital of a central potential. The nucleus has no physical source of a central potential, as an atom does, but an effective central potential comes about from the average force of all the other nucleons. Calculations typically assume the effective central potential to consist of harmonic oscillator and spin-orbit potential parts. The nucleons fill the orbitals, starting with those of lowest energy, with the Pauli principle allowing only one nucleon per orbital. The shell structure is a result of the large difference in energy between states of different principle quantum number. More realistic shell models include a residual two-

body interaction between the nucleons. To first order, nucleons in the filled shells or 'core' can be ignored in calculations because the Pauli principle restricts the possible final states of scattering to the unfilled states at high excitation energies. However, the nucleons in unfilled shells can interact, resulting in a 'mixing of states' in the open shell.

The nuclear shell model is surprisingly good at explaining binding energies, energy level schemes and other nuclear properties, especially for low A nuclei, but clearly it must have its limitations. Finding the region of validity of the shell model and understanding why it fails has proven to be fertile ground for investigation. One way of testing shell model wavefunctions is to check how well they predict the strengths of β and γ transitions. The simplicity of the operators in these transitions means that the strengths directly probe the wavefunctions of the initial and final states of the nucleus.

1.1 Beta decays and M1 Transitions

Nuclear β decays provide an ideal laboratory in which to investigate nuclear structure. In β^- (β^+) decays the weak interaction induces a nuclear transformation which is accompanied by the emission of an electron (positron) and an anti-neutrino (neutrino). The simplest example is the β decay of the neutron:

$$\mathrm{n} \rightarrow \mathrm{p} + \mathrm{e}^- + \bar{\nu}$$

The transformation changes the charge of the nucleus by $Z \rightarrow Z \pm 1$ which is equivalent to a unit change in the third component of isospin, T_3 (or T_z), and is therefore an isovector transition. Because the weak interaction is well known at this level, β decays can be used to study nuclear wavefunctions.

Two common types of β decay are known from selection rules. The first type is the 'Fermi' transition in which the nucleus undergoes no change in total angular momentum, J.

Δ J=0 (Δ L=Δ S=0) Fermi Selection Rule

The second type of transition involves a unit change in total angular momentum of the nucleus and is called a 'Gamow-Teller' (GT) transition.

Δ J = $\pm$1, 0 (no 0 $\rightarrow$ 0) GT Selection Rule

The parity of the nucleus does not change in either type of transition. The different selection rules are the results of the different couplings of the spins of the emitted electron and anti-neutrino. In other types of β decay, the so called 'forbidden' decays, the emitted β and ν can carry off orbital angular momentum as well as spin. The matrix elements of the nuclear parts of the Fermi and GT transitions are

$$M_F = < f || \sum_k t_k^{\pm} || i > \tag{1.1a}$$

$$M_{GT} = < f || \sum_k \boldsymbol{\sigma}_k t_k^{\pm} || i > \tag{1.1b}$$

where i and f denote the initial and final nuclear states including spin and isospin, t^+ (t^-) is the isospin raising (lowering) operator and $\boldsymbol{\sigma}$ is the Pauli spin operator. The sum is over all the nucleons in the nucleus. The strength of a β decay is defined as

$$B(F) = |M_F|^2 \tag{1.2a}$$

$$B(GT) = \frac{|M_{GT}|^2}{2J_i + 1} \tag{1.2b}$$

where J_i is the spin of the initial nucleus. These strengths are usually in units such that $B(F)$=1 and $B(GT)$=3 for the decay of the neutron.

Beta decay strengths for specific transitions can be found experimentally from the partial half-life of the decay (the half-life due to that branch of decay) and the energy spectrum of the emitted electrons or positrons. The relation is

$$(g_V)^2 B(F) + (g_A)^2 B(GT) = \frac{K}{ft} \tag{1.3}$$

where g_A and g_V are the weak interaction axial-vector and vector coupling constants, and

$$\frac{K}{(g_V)^2} = 6166 \pm 2 \text{ sec}$$

$$\frac{g_A}{g_V} = 1.260 \pm 0.008$$

and f is a phase space factor, t is the partial decay half-life and K is a constant [BW 85].

All the Fermi strength in the decay of a given nucleus is found in one transition. The total Fermi strength is given by

$$B(F) = N_i - Z_i \tag{1.4}$$

where N_i (Z_i) is the number of neutrons (protons) in the parent nucleus. Whereas all $B(F)$ is found in one transition, the GT strength is fragmented and much of it is outside the energy window of nuclear β decay [Ike+ 63]. The spin-dependent residual interaction spreads out the GT strength over several states. The total GT strength in a nucleus however obeys a sum rule [Gaa +80].

$$\sum_f B(GT)^- - \sum_f B(GT)^+ = 3(N_i - Z_i) \tag{1.5}$$

where the $GT^{\pm}$ operators are given in 1.1b, and the sum is over all final states.

Gamma decays can also be used to investigate nuclear wavefunctions. The simplest γ decay is the magnetic dipole (M1) transition involving states of the same parity which has an operator very similar to the GT operator. The selection rule for M1 transitions is

ΔJ= $\pm$1,0 no 0 $\rightarrow$ 0 M1 Selection Rule

The M1 matrix element contains pieces from the matrix elements of the spin '**s**' as well as orbital '**l**' angular momentum operators:

$$M_{M1} = (3/4\pi)^{1/2} < f|| \sum_i g_s \mathbf{s}_i + g_l \mathbf{l}_i ||i > \mu_N \tag{1.6}$$

where $\mathbf{s} = \boldsymbol{\sigma}/2$ and the g's are the spin and orbital g-factors for free-nucleons and the sum is over all nucleons. For isoscalar transitions g_s=0.880 and g_l=0.500, while for isovector transitions g_s=4.706 and g_l=0.500. M_{M1} has both isoscalar and isovector parts and the total matrix element is simply the sum. For strong transitions the M1 matrix element is dominated by the spin-flip isovector piece. The strength is defined as

$$B(M1) = \frac{|M_{M1}|^2}{2J_i + 1} \tag{1.7}$$

Magnetic dipole strengths are given in units of nuclear magnetons squared (μ_N^2). The major difference between the M1 and GT matrix elements is the orbital term which can interfere with the spin term. Another difference is found in the relativistic structure of the currents in the operators. The GT operator couples to axial-vector currents while the M1 couples to vector currents.

It is observed that β and γ decay strengths in nuclei are systematically less than those predicted by shell model calculations [BW 88,Tow 87]. This so called 'quenching' of strength has been the subject of much theoretical and experimental work. This is especially true in the *sd* shell (^{16}O–^{40}Ca) where a new universal interaction is expected to give good nuclear wavefunctions because of its success in reproducing experimental energy levels [Wil 84]. In *sd* shell nuclei typically only 60% of the predicted strength is seen. This is consistent with a value of $|g_A/g_V|_{eff}$ $\approx$ 1.0 in a nuclear medium. The different possible mechanisms of the quenching involve additional nuclear and sub-nuclear degrees of freedom, including meson exchange currents (MEC), which will be discussed in section 2.1.

Since much of the GT strength in a nucleus is inaccessible to β decay, complete studies of $B(GT)$ must be done in other ways. Recently it has been found that inelastic nucleon-nucleus scattering at intermediate energies, with charge exchange, is a good probe of β decay strength, seeing strength up to high excitation energies [BE 87].

1.2 Charge Exchange Reactions

The discovery of the Isobaric Analog Resonance (IAR) ($T=T_o \neq 0$, $\Delta S=0$, $\Delta L=0$) in 1961 by the $^{51}V(p,n)^{51}Cr$ reaction at $E_p = 14.5$ MeV gave the first indication that the isospin dependent structure of nuclei could be seen by N-nucleus scattering [AW 61]. The IAR contains almost all of the Fermi transition strength. Later, as higher energies became available, the resonance corresponding to the Gamow-Teller transitions (GTR) ($\Delta T=1$, $\Delta S=1$, $\Delta L=0$) was discovered, also by the (p,n) reaction [Doe+ 75].

The (p,n) reaction at intermediate energies came to be used in different ways. The first was to study the components of the nuclear interaction at intermediate energies. The great selectivity of the (p,n) reaction picks out only the central isovector spin-flip

$$V_{\sigma\tau}^{C}(\mathbf{r}_{ip})\boldsymbol{\sigma}_i \cdot \boldsymbol{\sigma}_p \boldsymbol{\tau}_i \cdot \boldsymbol{\tau}_p \tag{1.8a}$$

and non spin-flip

$$V_{\tau}^{C}(\mathbf{r}_{ip})\boldsymbol{\tau}_i \cdot \boldsymbol{\tau}_p \tag{1.8b}$$

pieces of the interaction at low momentum transfer, q. Here $\boldsymbol{\sigma}_i$ is the spin operator acting on the i_{th} nucleon in the nucleus and $\boldsymbol{\sigma}_p$ is the spin operator acting on the projectile nucleon, and the τ's are the isospin operators (τ=2t). If a known state can be identified from excitation energy, it can be found whether the transition involved is of the spin-flip type. If both Fermi and GT transitions can be resolved, the relative strengths can be compared in the same nucleus. From such experiments it was found that at intermediate energies the spin-flip piece of the interaction $V_{\sigma\tau}$ is larger than the non spin-flip piece V_{τ}, by as much as a factor of ten [Alf+ 86b]. One also finds that over the region 150–500 MeV the central isovector spin-flip piece of the NN interaction is quite flat so 0° cross sections can change very little with bombarding energy [Wat+ 89].

Other studies with the (p,n) reaction have shown a relationship between (p,n)

cross sections and $B(GT)$ and $B(F)$ for specific transitions [Tad+ 87].

$$\sigma_{pn}(q,\omega,A,E_p) = \hat{\sigma}^{-}_{GT}(A,E_p)F(q,\omega)B(GT) \tag{1.9}$$

where $\hat{\sigma}^{-}_{GT}(A,E_p)$ is the proportionality constant, $F(q,\omega)$ is a form factor such that $F(q,\omega) \rightarrow 1$ as $q,\omega \rightarrow 0$ and ω is the total energy loss $\omega = Q - E_x$. This is not unexpected because the central isovector terms of the nucleon-nucleon potential responsible for the low q non spin-flip and spin-flip isovector transitions (1.8a and 1.8b) are closely related to the Fermi and GT β decay operators (1.1a and 1.1b). The (p,n) reaction induces the same transitions as β decay but they can also, in principle, see all the GT strength in a nucleus because the energy constraints are removed. By measuring the cross section of a known transition it's proportionality to $B(GT)$ or $B(F)$ can be empirically determined. This proportionality was found to depend on A and smoothly on E_p. The relationship between σ_{pn} and $B(GT)$ has also been studied theoretically within the framework of the distorted wave impulse approximation (DWIA) description of charge exchange reactions (see section 2.2).

The (p,n) reaction sees only the strength of transitions analogous to those involving β^- operator (GT^-). The related (n,p) reaction can be used to probe the β^+ strength (GT^+). Both are needed to test the GT sum rule (1.5). For N=Z nuclei the (n,p) reaction probes the same strength as the (p,n) reaction. For N>Z nuclei the (n,p) reaction is even more selective than the (p,n) reaction because for target nuclei with ground state isospin of $T_o = (N-Z)/2$ only states of isospin $T=T_o+1$ are populated. Since the (n,p) reaction is related to the β^+ decay it can also probe strengths of more general interest such as those which are important for $\beta\beta$ decay and weak processes in supernovae.

Spin-isospin excitations in nuclei can been studied by other probes. The (π^-,γ) reaction has been used to probe isovector excitations, especially in the p shell, but are limited by having inherently large momentum transfer and low particle emission threshold. The (p,p') reaction at low q has also be used and whereas the resolution in such studies is generally good enough to resolve individual states,

this reaction lacks the selectivity of charge exchange reactions. The cross sections of the three nucleonic reactions for the analog transition are related by a Clebsch-Gordan coefficient, so that for T_i=0 and T_f=1, $\sigma_{pn} = \sigma_{np} = 2\sigma_{pp}$. Both electron scattering at 180° and (γ, γ') reactions can probe the related isovector magnetic dipole transition strength. The transitions seen by the different probes are shown in figure 1.1.

1.3 Experiment 474

A survey has begun at TRIUMF to measure $B(GT)$ in *sd* shell nuclei using the (n,p) reaction at intermediate energies to study the systematics of quenching in the *sd* shell. The $B(GT)$ is also compared with $B(M1)$ extracted from high resolution (e, e') to gain insight into the role of orbital and MEC contributions to the M1 matrix element [Ric 89]. Calculations using the universal *sd* shell interaction predict the interference between the spin and orbital terms is strongest low in the *sd* shell [KM 83]. Other calculations predict that the contribution from MEC does not vary much across the shell [Bro 87]. In ^{20}Ne the interference pushes almost all of the M1 strength into a single state at 11.26 MeV while the Gamow-Teller strength is spread over several states between E_x=0–10 Mev in ^{20}F . Bendel *et al.*have measured the $B(M1)$ in ^{20}Ne by (e, e') and see that it is indeed in a single peak [Ben+ 71]. A recent (p,p′) experiment has measured the GT strength in ^{20}Ne, but was hampered by contamination from the windows, and the inability to distinguish between T=0 and T=1 states unambiguously [Wil+ 87]. The (p,n) reaction was also used to measure $B(GT)$ in ^{20}Ne with results forthcoming [And 89].

TRIUMF experiment 'E474' measured cross sections of the ^{20}Ne(n, p)^{20}F reaction at E_n = 198 MeV for 5 angles from θ_{lab} = 0° to 15°. A high pressure (n,p) gas target was developed for use in the TRIUMF charge exchange facility for ^{20}Ne and other gaseous targets. The subject of this thesis is the experimental details and the analysis of the results of E474. Chapter 2 discusses theoretical details

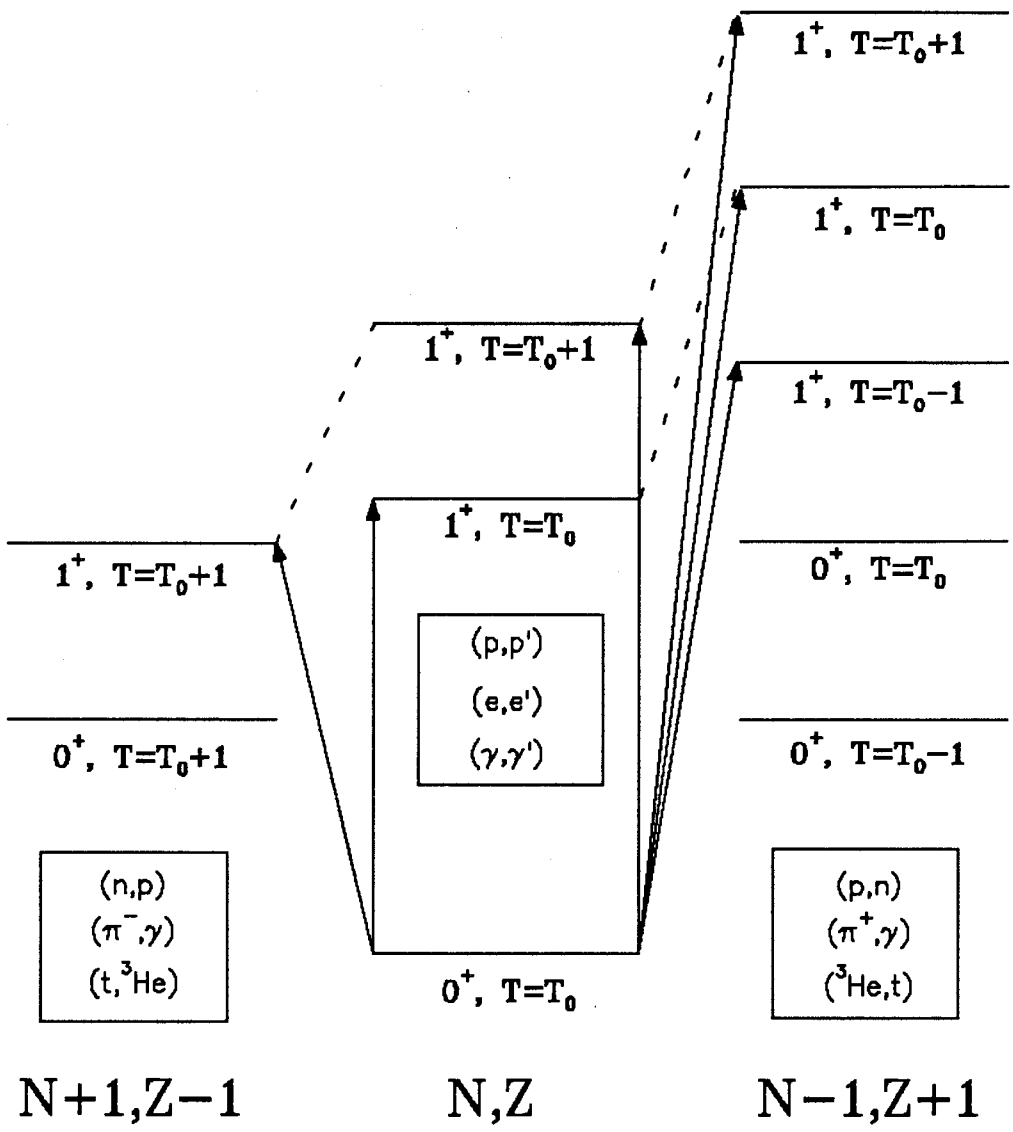

Figure 1.1: Spin-isospin excitations studied with different probes

of the shell model and charge exchange reactions. Chapters 3 and 4 describe the TRIUMF charge exchange facility with a detailed discussion of the high pressure gas target which was developed for this experiment. Chapters 5 and 6 describe the analysis of the data and the extracted results.

Chapter 2

Theoretical Considerations

Nucleon-nucleus scattering at intermediate energies can be used to study both nuclear structure and nuclear reactions. If either the structure or the reaction is well known, information on the other can be found. The shell model is used to calculate the wavefunctions for nuclear structure. If the wavefunctions are to be investigated the reaction theory must be well known. At intermediate energies N-nucleus scattering is well described in the framework of the distorted wave impulse approximation (DWIA).

2.1 Nuclear Structure

The full nuclear Hamiltonian is

$$\mathcal{H} = \sum_i T(\mathbf{r}_i) + \sum_{i<j} V(\mathbf{r}_i, \mathbf{r}_j) \tag{2.1}$$

where i and j label the nucleons, $T(\mathbf{r}_i)$ is the single particle kinetic energy operator, and $V(\mathbf{r}_i, \mathbf{r}_j)$ is the two-body NN potential. This many-body problem cannot be solved exactly so a model must be made. The shell model assumes that the strong two-body interaction, $V(\mathbf{r}_i, \mathbf{r}_j)$, can be approximated as a strong central potential plus a weak residual two-body interaction.

$$\mathcal{H} \approx H_1(\mathbf{r}_1) + H_{12}(\mathbf{r}_1, \mathbf{r}_2) \tag{2.2}$$

where $H_1(\mathbf{r}_i) = T(\mathbf{r}_i) + U(\mathbf{r}_i)$ is the one-body Hamiltonian, $U(\mathbf{r}_i)$, the central potential and $H_{12}(\mathbf{r}_1, \mathbf{r}_2) = V(\mathbf{r}_1, \mathbf{r}_2) - U(\mathbf{r}_1)$ is the weak residual interaction and is small enough to treat by perturbation theory.

Calculating the nuclear wavefunction requires the diagonalization of both the strong central and the weak two-body interactions. First single particle states are found by diagonalizing the one-body Hamiltonian, H_1. This set of states is then truncated to include only states in, and sometimes above, the unfilled shell. The residual two-body interaction is diagonalized in the truncated basis set, mixing the single particle states, to give the many-particle wavefunction. For *sd* shell calculations the new universal *sd* shell interaction is commonly used [Wil 84]. It consists of one and two-body interactions, the interaction strengths having a mass dependance of $< V > (A) =< V > (A = 18)(A/18)^{-0.3}$, to include first order configuration mixing in the whole $0d_{5/2}$-$1s_{1/2}$-$0d_{3/2}$ basis. It uses 'model independent' parameters consisting of single particle energies and two-body matrix elements fit to 447 pieces of *sd* shell binding energy and excitation energy data. It has been very successful in reproducing experimental energy level schemes and some weak and electromagnetic data [BW 88].

Modern shell model calculations are done with computer codes. Modern codes, using readily available computer power, can do very large scale diagonalization in a reasonable time. One widely used code is OXBASH [Etc+ 85]. OXBASH works in occupancy number formalism and uses an m-scheme Slater determinant to define a basis set for a specific number of particles and a particular J_z and T_z. Out of this basis, states with good J and T are projected and then the Hamiltonian matrix is constructed. The Lanczos diagonalization scheme is then used to find the eigenvalues and eigenfunctions. Transition densities can then be found from the final many-body wavefunctions for both one and two-body operators. The OXBASH code can be used with a variety of interactions and basis sets.

Although the universal *sd* shell interaction can reproduce energy levels well, it

overestimates the M1 and GT strength by about 30–40%. Additional nuclear and subnuclear degrees of freedom have been used to explain the missing strength in all mass regions. These include core polarization, Δ-isobar excitations, and meson exchange currents. Towner & Khanna, Arima *et al.*, and Oset & Rho have calculated quantitative values for the different contributions [TK 83,Tow 87,Ari+ 88,OR 79]. The largest corrections affect the strength of the spin operator.

(i) Core polarization

Even modern shell models are limited to considering the mixing of states only in the open shell. This mixing automatically takes into account the so called 'first order configuration mixing'. The states in the core shells are assumed to be unaffected by the residual interaction. Higher order configuration mixing or 'core polarization' (CP) takes into account the excitation of nucleons in the core shells. These nucleons can mix with states in and above the unfilled shells at many $\hbar\omega$ excitation. The contribution due to CP is calculated using perturbation theory with an effective interaction. The effect of CP is to quench the strength of the spin operator by spreading it out in a small background at high excitation which would be undetectable in current experiments. Towner & Khanna calculated the second order core polarization correction for closed-shell-plus (or minus)-one nucleon. The calculations of Towner & Khanna and Arima *et al.*predict a large quenching of the spin operator in isovector M1 and the GT strength (about 25% for A=39). Both sets of calculations show this as the major contribution to quenching.

(ii) Δ-Hole Excitations

The nucleons in the nucleus also have degrees of freedom. An isovector spin-flip interaction can couple the nucleon (J=1/2, T=1/2) to the $\Delta(1232)$ isobar(J=3/2, T=3/2). This excitation is readily seen in intermediate energy NN and π-N scattering. The Pauli blocking which reduces much of the strength in neutron rich

nuclei does not affect the strength of Δ excitations, because the Δ has a different set of quantum numbers. Although the direct excitation of the Δ involves higher energy, the N-Δ coupling might be quite strong. Evidence for the excitation of the Δ in low and medium energy nuclear reactions can be sought by comparing the quenching of isovector processes with that of isoscalar processes [Saw 87]. On the theoretical front, the size and direction of the contribution from Δ-hole correlations is a point of present controversy. For example, for the correction to the spin operator in GT strength for A=39 Towner & Khanna calculate $\delta_s(GT)$=–0.038 compared to 0.004 from Arima *et al.*and –0.15 from Oset & Rho [TK 83,Ari+ 88,OR 79].

(iii) Meson Exchange Currents

Since the 1930's it has been assumed that the NN force is carried by the exchange of mesons (see 2.2.1). This means that the mesons are also constituents of nuclei and have an effect on a probe of the nuclear wavefunctions. The MEC is different in that it depends on the relativistic structure of the currents in the interaction. For GT transitions the currents are axial-vector while they are vector for the isovector M1 operator. The corrections to the calculated GT strength come largely from the $\rho - \pi$ meson exchanges and are small (on the order of q/M where M is the nucleon mass). For M1 strength the meson exchange currents are dominated by one-pion-exchange and are of order unity. MEC enhance the spin operator strength and cancel some of the quenching due to CP and the Δ. The calculations of Towner & Khanna and Arima *et al.*predict that the enhancement of the spin operator in the GT matrix element is negligible but in the M1 matrix element it is about 12% for A=39. Thus the quenching of $B(M1)$ should be less than that of $B(GT)$. A systematic difference between the quenching of $B(M1)$ and $B(GT)$ could be evidence of MECs in nuclei.

The contributions due to the above mechanisms are given in the form of cor-

rections to the general rank one tensors **s**, **l**, and **p** where $\mathbf{p} = (8\pi)^{1/2}[\mathrm{Y}^{(2)} \otimes \mathbf{s}]^{(1)}$. The corrections are in terms of additional 'δ' parameters. Whereas the free-nucleon operators are:

$$Op(GT, free) = |g_A/g_V|\mathbf{s} \tag{2.3a}$$

$$Op(M1, free) = g_s\mathbf{s} + g_l\mathbf{l} \tag{2.3b}$$

The effective operators are

$$Op(GT, eff) = Op(GT, free) + |g_A/g_V|[\delta_s(GT)\mathbf{s} + \delta_l(GT)\mathbf{l} + \delta_p(GT)\mathbf{p}] \tag{2.4a}$$

$$Op(M1, eff) = Op(M1, free) + g_s[\delta_s(M1)\mathbf{s} + \delta_l(M1)\mathbf{l} + \delta_p(M1)\mathbf{p}] \tag{2.4b}$$

The M1 operator has both isoscalar and isovector parts, but the GT operator is purely isovector.

The above definitions and parametrizations are those of Brown & Wildenthal, who have found empirical values for the parameters by fitting existing *sd* shell weak and electromagnetic data to the effective operators [BW 87]. The empirically fit corrections are compared to the calculated corrections of Towner & Khanna and Arima *et al.*for A=39 in fig 2.1. In principle the corrections should be done to a many-body wavefunction, but analysis shows little need for them if a mass dependence of $\delta(A) = \delta(A = 28)(A/28)^{0.35}$ is included. Some of the empirically fit parameters match the calculated ones reasonably well, but not all. The empirical operators can be used in conjunction with the universal *sd* shell interaction to calculate $B(GT)$ and $B(M1)$. The testing of these predictions can give insight into the causes of quenching in the *sd* shell.

2.2 Nucleon-Nucleus Scattering

At intermediate energies N-nucleus scattering is best described in terms of the DWIA. The impulse approximation implies that N-nucleus scattering involves the incident nucleon interacting with only one target nucleon. The scattering is mediated by the free NN interaction. The total nucleus only distorts the incoming

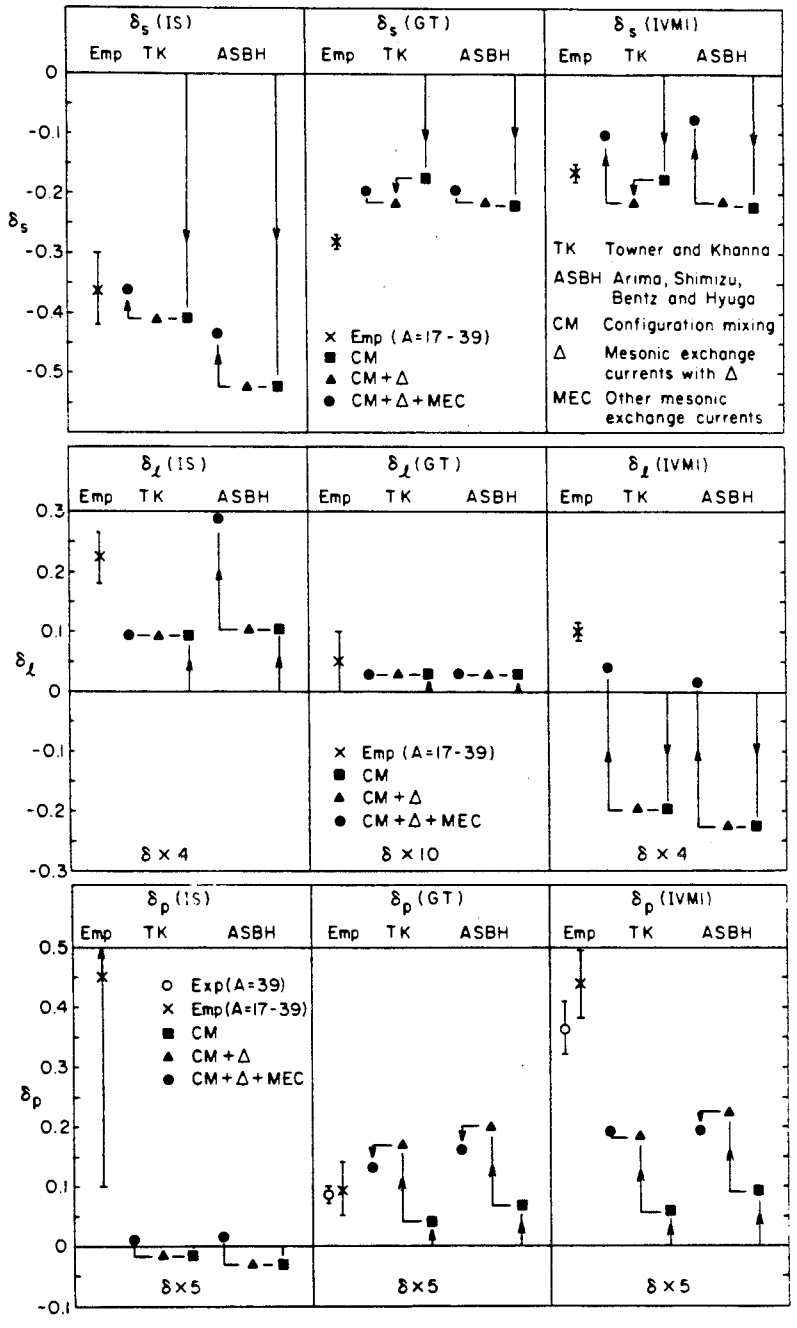

Figure 2.1: Corrections from fitting to the empirical operators compared to calculated corrections for A=39. From reference BW87.

and outgoing waves. The DWIA simply factors the scattering into a reaction part, which has the same coupling as free NN interactions, and a nuclear structure part.

2.2.1 The Nucleon-Nucleon Interaction

In general the NN interaction is very complex. The physically possible terms in the interaction involve Lorentz scalars which are formed from combinations of different operators. Of the 18 possible Lorentz scalars, only five are linearly independent and invariant under continuous and discrete transformations as is required for strong interactions. These five scalars can also be isoscalar and isovector, so there are a total of ten possible terms. Ignoring the negligible quadratic spin-orbit term, the NN interaction can be written as:

$$\begin{aligned} V_{ip} = V_0^C(\mathbf{r}) + V_\sigma^C(\mathbf{r})\boldsymbol{\sigma}_i \cdot \boldsymbol{\sigma}_p + V_\tau^C(\mathbf{r})\boldsymbol{\tau}_i \cdot \boldsymbol{\tau}_p + V_{\sigma\tau}^C(\mathbf{r})\boldsymbol{\sigma}_i \cdot \boldsymbol{\sigma}_p \boldsymbol{\tau}_i \cdot \boldsymbol{\tau}_p \\ + V^{LS}(\mathbf{r})\mathbf{L} \cdot \mathbf{S} + V_\tau^{LS}(\mathbf{r})\mathbf{L} \cdot \mathbf{S}\boldsymbol{\tau}_i \cdot \boldsymbol{\tau}_p \\ + V^T(\mathbf{r})S_{ip} + V_\tau^T(\mathbf{r})S_{ip}\boldsymbol{\tau}_i \cdot \boldsymbol{\tau}_p \end{aligned} \tag{2.5}$$

where $\mathbf{L} \cdot \mathbf{S}$ is the usual spin-orbit operator, with

$$\mathbf{S} = \frac{1}{2}(\boldsymbol{\sigma}_i + \boldsymbol{\sigma}_p)$$

S_{ip} is the usual tensor operator,

$$S_{ip} = 3(\boldsymbol{\sigma}_i \cdot \hat{r})(\boldsymbol{\sigma}_p \cdot \hat{r}) - \boldsymbol{\sigma}_i \cdot \boldsymbol{\sigma}_p$$

and $\mathbf{r} = \mathbf{r}_{ip}$ the distance between the i^{th} target nucleon and the incident projectile p. The NN interaction can be found from physical first principles, a 'microscopic interaction', or fit to the experimental data, an 'effective interaction'.

The underlying physical principle in the NN interaction is meson exchange, which is analogous to photon exchange in quantum electrodynamics. Yukawa first postulated this mechanism in 1935 giving the range dependent part of the potential

as,

$$V(r) = \frac{Ve^{-\mu r}}{\mu r} \tag{2.6}$$

where μ is the range factor which is related to the mass of the meson. Yukawa assumed there was one type of meson, and one exchange involved. The pion had properties similar to the meson Yukawa expected and one-pion-exchange was reasonably successful in describing the long range part of the NN force.

Not all the properties of the NN interaction can be explained by the exchange of only one pion. Most modern microscopic potentials (such as the Paris and Bonn potentials) recognize three distinct regions of the interaction: an long range part, a medium range attraction and a short range strong repulsion. The interaction in each of these regions is due to the exchange of one or more different mesons with different types of couplings. At long range the contribution from the pseudoscalar pion is large and is mainly an isovector tensor force. The intermediate range attraction is largely isoscalar, spin-orbit and is provided by the exchange of the hypothetical scalar 'σ' meson. While no scalar meson has been found in the predicted mass region of the σ it is believed that the scalar character comes from the exchange of two pions in an s-state. The short range repulsion which is largely central is due to the heavy vector mesons, the ω (isoscalar) and the ρ (isovector).

Although the microscopic potentials have had some limited success, effective interactions are still best for reproducing experimental data. One of the most commonly used is the Love-Franey effective interaction [LF 81,FL 85]. This interaction is parametrized in each NN channel in terms of the superposition of Yukawa terms (2.6) for the central and spin-orbit pieces and r^2 x Yukawa terms for the tensor piece. These parameters are fit to the free NN scattering amplitudes from the Arndt phase-shift analysis [AS 84]. This is done by converting the scattering amplitudes to t-matrices, which are related simply by a kinematic factor, and assuming a finite range form for the interaction. The fits are done at five different ranges. The LF interaction is widely used in DWIA calculations.

2.2.2 DWIA

If the NN interaction is known, scattering observables can be calculated using the DWIA. Cross sections can be calculated using the T-matrix by the standard direct reaction formula

$$\frac{d\sigma}{d\Omega} = (\frac{\mu}{\pi\hbar^2})^2 \frac{k_i}{k_f} \frac{1}{2} \sum \frac{|T|^2}{2J_i + 1} \tag{2.7}$$

where μ is the relativistically reduced energy, the k's are wave numbers, and the sum is over all the final nuclear states.

In the distorted wave theory, the transition matrix is given by

$$T^{DW} = < \chi_f^{(-)}, \Psi_F | \sum_i V_{ip} | \chi_i^{(+)}, \Psi_I > \tag{2.8}$$

where $\chi_i^{(+)}$ ($\chi_f^{(-)}$) is the initial, incoming (final, outgoing) distorted wave of the projectile and Ψ_I (Ψ_F) is the initial (final) nuclear state. If V_{ip} is expressed in momentum space,

$$V_{ip} = \frac{1}{(2\pi)^3} \int d^3q e^{-i\mathbf{q}\cdot(\mathbf{r}_i - \mathbf{r}_p)} V_{ip}(\mathbf{q}) \tag{2.9}$$

the transition matrix becomes

$$T^{DW} = \sum_\alpha \int d^3q D_\alpha(\mathbf{k}, \mathbf{k}'; \mathbf{q}) V_\alpha(\mathbf{q}) \rho_{FI}^\alpha(\mathbf{q}) \tag{2.10}$$

where α represents the different pieces of the NN interaction, α = scalar, τ, $\sigma\tau$, tensor, etc. The transition amplitude is now in terms of pieces describing the interaction, $\mathrm{V}_\alpha(\mathbf{q})$, the distortions, $\mathrm{D}_\alpha(\mathbf{k}, \mathbf{k}'; \mathbf{q})$, and the nuclear transitions, $\rho_{FI}^\alpha(\mathbf{q})$.

In charge exchange reactions the interactions are purely isovector so, ignoring the weak spin-orbit piece, the NN interaction can be written as

$$V_{ip}(\mathbf{q}) = [V_\tau(\mathbf{q}) + V_{\sigma\tau}(\mathbf{q}) \boldsymbol{\sigma}_i \cdot \boldsymbol{\sigma}_p - V_\tau^T(\mathbf{q}) S_{ip}(\hat{q})] \boldsymbol{\tau}_i \cdot \boldsymbol{\tau}_p \tag{2.11}$$

where $S_{ip}(q) = [3(\boldsymbol{\sigma}_p \cdot \hat{q})\hat{q} - \boldsymbol{\sigma}_p] \cdot \boldsymbol{\sigma}_i$, $\hat{q} = \mathbf{q}/q$. At low momentum transfers $\mathrm{V}_{\sigma\tau}^C(\mathbf{q})$ and $\mathrm{V}_\tau^C(\mathbf{q})$ dominate in spin-flip and non spin-flip isovector excitations, while at larger momentum transfers ($q \geq$ 1fm^{-1}) the tensor piece, $V_\tau^T(\mathbf{q})$, dominates the spin-flip pieces.

The distortion factor, $D_\alpha(\mathbf{k},\mathbf{k}';\mathbf{q})$ is defined as

$$D_\alpha(\mathbf{k},\mathbf{k}';\mathbf{q}) = \frac{1}{(2\pi)^3} < \chi^{(-)}_{f,\mathbf{k}'} | e^{-i\mathbf{q}\cdot\mathbf{r}_p} Op_\alpha(\mathbf{q}) | \chi^{(+)}_{i,\mathbf{k}} > \tag{2.12}$$

where $Op_\alpha(\mathbf{q})$ is the operator involved in a piece of the interaction ($\boldsymbol{\tau}$, $\boldsymbol{\sigma\tau}$ etc...). The distorted waves can be generated using the Schrodinger equation with a complex optical potential

$$\{\nabla^2 + k^2 - (2\mu\hbar^2)[U_{opt}(\mathbf{r}) + U_{coul}(\mathbf{r})]\}\chi_{\mathbf{k}}(\mathbf{r}) = 0 \tag{2.13}$$

where $U_{coul}(\mathbf{r})$ is a Coulomb potential and $U_{opt}(\mathbf{r})$ is the complex optical potential

$$U_{opt}(\mathbf{r}) = V_o f_R(r) + iW_o f_I(r) \tag{2.14}$$

where $U_{opt}(\mathbf{r})$ can have scalar and spin-orbit parts. The f_is are the shapes of the potential well, often the Woods-Saxon forms. The parameters of the optical potential are found empirically from elastic scattering data.

Numerically the distortion factor can be calculated as simply the ratio of the cross sections calculated by DWIA for a certain q and energy, and the cross section calculated by plane wave theory PWIA, i.e.

$$D_\alpha = N^D_\alpha = \sigma(DW,q,E)/\sigma(PW,0) \tag{2.15}$$

The nuclear transition density, $\rho^\alpha_{FI}(\mathbf{q})$, for each operator, is defined as

$$\rho^\tau_{FI}(\mathbf{q}) = < \Psi_F | \sum_i \boldsymbol{\tau}_i e^{\mathbf{q}\cdot\mathbf{r}_i} | \Psi_I > \cdot < n|\boldsymbol{\tau}|p > \quad \text{Fermi Transition} \tag{2.16a}$$

$$\rho^{\sigma\tau}_{FI}(\mathbf{q}) = < \Psi_F | \sum_i \boldsymbol{\sigma}_i\boldsymbol{\tau}_i e^{\mathbf{q}\cdot\mathbf{r}_i} | \Psi_I > \cdot < n|\boldsymbol{\sigma\tau}|p > \quad \text{GT Transition} \tag{2.16b}$$

As $q \to 0$ the transition densities become proportional to the Fermi and GT matrix elements.

At $q = 0$ the cross section becomes

$$\frac{d\sigma}{d\Omega}(q=0) = (\frac{\mu}{\pi\hbar^2})^2 \frac{k_i}{k_f}[N^D_\tau |J_\tau|^2 B(F) + N^D_{\sigma\tau}|J_{\sigma\tau}|^2 B(GT)] \tag{2.17}$$

where the N^Ds are the distortion factors, and $J_{\sigma\tau}$ and J_τ are the volume integrals of the $(\sigma\tau)$ and (τ) components of the NN interaction. The proportionality between cross section and β decay strengths is clear. For the (n,p) reaction the cross sections are given by

$$\frac{d\sigma_{np}}{d\Omega}(q=0) = (\frac{\mu}{\pi\hbar^2})^2 \frac{k_i}{k_f} N^D_{\sigma\tau} |J_{\sigma\tau}|^2 B(GT_+) = \hat{\sigma}^+_{GT} B(GT) \qquad (2.18)$$

Using DWIA a theoretical value for $\hat{\sigma}^+_{GT}$ can be calculated.

Recent experimental work at the Indiana University Cyclotron Facility (IUCF) and TRIUMF has empirically verified the relationship between cross section and $B(GT)$ for both (p,n) and (n,p) reactions for incident energies up to and beyond 200 MeV [Tad+ 87,Jac+ 88]. These results were compared with those calculated using DWIA and the theory underpredicts the cross sections by 10–20%. There is still much controversy concerning the dependence of $\hat{\sigma}$ on A. Because of the importance of the value for quantitatively extracting $B(GT)$ and $B(F)$ from charge exchange reactions this must investigated.

Chapter 3

Experimental Technique

3.1 The TRIUMF Cyclotron

The TRIUMF cyclotron is a six-sector isochronous cyclotron which accelerates H^- ions to energies up to 520 MeV. The energy is continuously variable from 183 to 520 MeV with 0.1–99.9% duty factor. When operated with a high duty factor large currents can be achieved, up to 140μA for unpolarized running and 600 nA for polarized. The momentum spread in the beam is typically 0.15%$\Delta p/p$ which corresponds to ΔE $\approx$0.6 MeV for E=200 MeV. Two ion sources are presently being used, one which produces polarized beam and a second which produces unpolarized and two new sources are presently being developed. A 300 keV injection line is used to accelerate and inject the H^- ions. Protons are extracted by stripping two electrons from each H^- using a carbon foil. Proton beams are transported to two large experimental halls, one for nucleon experiments and the other for pion and muon experiments. The different beams are carried through the beam pipes at high vacuum and are bent and focussed by a series of dipole and quadrupole magnets, respectively. The magnets are 'tuned' for beam transport and focus remotely using a series of retractable beam profile monitors located near each beam element. Although a theoretical tune can be calculated, instabilities and uncertainties in the beam optics require empirical fine-tuning.

For an achromatic beam tune, the beam is focused to a point at the target,

whereas for a dispersed tune the dipole bending magnets transform the momentum dispersion to spatial dispersion. This spatial dispersion is necessarily along the plane of the benders (the horizontal or 'Y' direction). For dispersion matching to the medium resolution spectrometer it is necessary to transform the dispersion to be in the bend plane of the spectrometer (the vertical or 'X' direction) which is 90° to the plane of the benders. This transformation is accomplished by the 'Twister' which consists of six independently variable quadrupole magnets.

3.2 The Medium Resolution Spectrometer

The medium resolution spectrometer (MRS) system consists of a quadrupole and a dipole magnet located at the end of proton beamline 4B. The set-up can be seen in figure 3.1. The quadrupole magnet is located just upstream of the dipole magnet. It focuses the beam into the dipole magnet which bends it vertically through 60° to a set of four vertical drift chambers (VDCs) located at the focal plane. Above the VDCs are a series of scintillators PD_{0-9} which can be put in the trigger to define the active region of the focal plane. Behind these are two consecutive large area scintillator paddles S1 and S2. Above the focal plane of the MRS is a polarimeter which can measure the polarization of scattered protons or deuterons. Particle identification is provided by the time of flight between the front end chambers and PD_{0-9} and by the sum of the energy loss ($\Delta E/E$) in PD_{0-9}. The solid angle acceptance of the spectrometer is about 2.5 msr. Ray-tracing is provided before the dipole by a set of front end chambers (FECs) which are located behind the target and after the dipole by the VDCs.

Front end ray-tracing in the charge exchange facility ('CHARGEX') is provided by two FECs (FECM and FEC∅). Each FEC has two pairs of wire planes, one pair in the direction of the bend plane ('X' direction), and one pair perpendicular to it ('Y' direction). The wire planes consist of sixteen pairs of alternating anode and cathode wires which can cover an area of 8 cm by 8 cm. The planes are staggered

by 1/2 wire spacing to eliminate left-right ambiguity. To reduce the rates in the FECs the active areas can reduced by inserting insulating kapton masks between the planes. The FECs have a resolution of <0.5 mm in both X and Y planes.

The momentum of a particle is determined by measuring its position at the focal plane of the spectrometer. The focal plane position measurement is done by the VDCs. Four VDCs are used, two in the direction of the bend plane (X1 and X2) and two at 30° to the bend plane (U1 and U2). Together they can give information in X and Y directions. The resolution of the VDCs in the bend plane is $\sim$ 150 μm. The VDCs are long in the X direction (30 cm x 105 cm) and allow for a large momentum bite ($\Delta p/p \simeq .15$) to be measured.

3.3 The CHARGEX Facility

The study of charge exchange reactions above 50 MeV has generally explored the (p,n) channel. The main facilities for this are at the Los Alamos Meson Facility (LAMPF) and IUCF. Both these facilities use neutron time of flight (NTOF) to measure the outgoing neutron energy. At TRIUMF NTOF techniques cannot be used for charge exchange reaction measurements because of both the beam time structure and the limited space. The TRIUMF charge exchange facility exploits the high beam intensity to study charge exchange reactions by using a two reaction process where one of the reactions is well known. The object is to have protons in both the initial and final states where they can be momentum analyzed in the existing MRS. Such a setup allows all three hadronic isovector excitation channels ((p,n) (p,p′) and (n,p)) to be measured at one facility, including the only existing facility to measure (n,p) reactions at intermediate energies. Proton inelastic scattering, (p,p′), reactions have been measured at TRIUMF for some time and small angle spin-flip excitations have been studied using the focal plane polarimeter which can measure $S_{nn'}$, the spin-flip probability, and thus separate natural parity (ΔS=0) from spin-flip transitions (ΔS=1). The good resolution

(about 140 keV FWHM) in some cases allows the separation of isoscalar and isovector states.

The charge exchange facility was developed to do studies complimentary to the (p,p′) work. Certainly the two charge exchange reactions would not have as good resolution as the (p,p′) but this is compensated for by the absence of strong natural parity excitations. For the (p,n) measurements a recoil-proton method is used, where a proton hits the target of interest and creates a neutron. The neutron then reacts with a hydrogen in a secondary target (CH_2 or liquid scintillator) at low q producing a proton of nearly the same energy which goes on to be momentum analyzed in the MRS. For (n,p) reactions a nearly monoenergetic neutron flux is produced by the ^{7}Li(p, n) reaction and the outgoing proton is momentum analyzed by the MRS. Both reactions can be measured with only minor modifications to the basic setup. The facility allows measurements of angles from $\theta_{lab} = 0°$, which is important for studies of Gamow-Teller excitations, to higher angles which allows the study of states with higher multipolarity.

3.3.1 The (p,n) Mode

In the (p,n) configuration the (p,n) target (T_{pn}) is positioned at the MRS pivot. It is mounted on a six-position target ladder contained in a scattering chamber near the poles of a compact sweeping magnet. The proton beam that passes through this target is bent by the sweeping magnet through 20° to clean-up quadrupole magnets which focus the beam into the ARGUS beamdump which acts as a Faraday Cup for beam integration. If the beam is momentum dispersed vertically a thin horizontal strip target can be used to pick out a small part of the momentum. This can decrease the contribution to the resolution from momentum spread in the beam and lead to better overall resolution. This technique has the drawback of increasing the beam that goes into the beamdump, which limits the currents that can be run, decreasing the (p,n) reaction rate.

To stop scattered protons from being bent by the sweeping magnet to the (n,p) target (T_{np}), a Tungsten alloy proton blocker is placed in the scattering chamber just following the (p,n) targets. At MRS angles larger than 5° additional absorbers of copper or lead can be added at the exit of the magnet. Protons which still scatter or convert before T_{np} are detected in a thin veto scintillator (VS) and used in the trigger to reject events involving protons. At low currents the VS would be sufficient to reject all the charged particles.

The neutrons from T_{pn} travel 92 cm downstream to a hydrogenous target (T_{np}) which efficiently converts the proton to a neutron using the strong H(n,p) reaction at 0°, which has a laboratory cross section of $\simeq$53 mb/sr at E_n=200 MeV. The target is usually in the form of a recoil scintillator which is a 2.54 cm x 2.54 cm x 6.0 cm glass vessel containing BICRON BC513 liquid scintillator of a large hydrogen density. The signal from the scintillator is measured and used to correct for the energy loss in it. Alternately the (n,p) segmented box has been used with 6-CH_2 targets (see below). The segmentation of this target also allows for energy loss corrections. The recoil protons from T_{np} are then analyzed in the MRS.

Absolute cross sections are determined by having a ^{7}Li target in the (p,n) ladder and measuring the ^{7}Li cross section at each angle under the same conditions. By knowing the total beam current for both the target and the ^{7}Li runs the target cross sections can be normalized to the known ^{7}Li cross sections [Wat+ 89].

3.3.2 The (n,p) Mode

For the (n,p) configuration the (p,n) target and sweeping magnet are moved 92 cm upstream and a segmented (n,p) target box is positioned over the MRS pivot. A target for neutron production is positioned at (T_{pn}). The target used is a foil or strip of ^{7}Li. ^{7}Li has a large (p,n) cross section at 0°, ($\approx$35$\pm$3 mb/sr for E_p=50–400 MeV [Wat+ 89]). The (p,n) reaction populates the ground state and the first excited state (429 keV) of ^{7}Be and has a weak tail due to the continuum response

which is about 1% of the integrated peak area per MeV. The width of this doublet is a factor in limiting the best possible resolution. The best resolution is found using a dispersed beam tune and a narrow ^{7}Li strip and/or a thinner target (110 mg/cm^2). For E474 the major concern was for maximum count rate so a thick (220 mg/cm^2) ^{7}Li foil was used with an achromatic beam tune. These contribute 800 and 600 keV, respectively, to the resolution, giving, in quadrature, a total resolution of 1.0 MeV.

From T_{pn} the neutrons travel 92 cm downstream to the center of the (n,p) target box where the reactions of interest take place. At the center of the target box the neutron flux from a current of I_p=500 nA is about 2.4x10^5 s^{-1} cm^{-2} if the thick 220 mg/cm^2 ^{7}Li (p,n) target is used. The (n,p) target box is segmented to give maximum target thickness with minimum degradation of resolution due to energy loss in the target. Since the target layer of the reaction is known the energy loss in subsequent targets can be corrected for. The segmentation also allows the simultaneous measurement of different targets and rejection of reactions in the entrance or exit windows. Such a target box for solid targets has been in use for some time and is described elsewhere [Hen+ 87]. For E474 a segmented target box for gas targets was built and is described in chapter four.

The target box for solid targets consists of six solid targets (T_1 to T_6) sandwiched between detector planes. There are eight such wire planes. Before the first target are two planes Y_V and $Y_{V'}$, which form a double-plane veto, to reject events from the front window. Then there are six more planes, one after each target, to allow for target identification. Each target is mounted on a wheel that allows for a total of three different target stacks to be used. The most common stacks include: one with four solid targets of interest followed by an empty target position and a CH_2 target in the last position for target normalization. The second stack consists of six CH_2 targets which are used to normalize each individual target position taking wire plane efficiencies and position dependent effects (such as different neu-

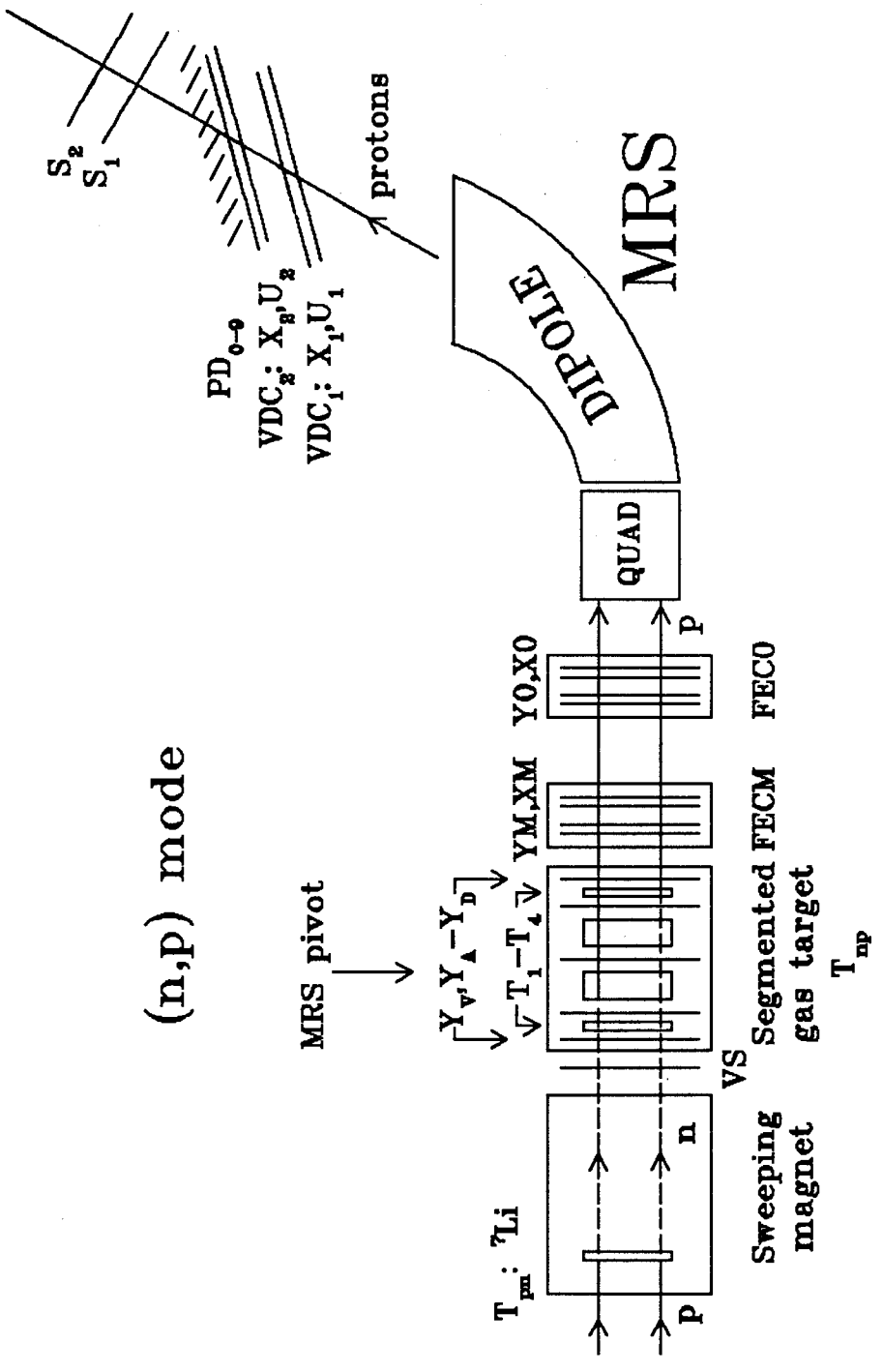

Figure 3.1: The CHARGEX facility in (n,p) mode with the gas target.

tron flux and acceptance) into account. The third stack is used to measure the backgrounds from the wire chambers and the chamber gas. It contains five empty target positions followed by a CH_2 target to normalize the neutron beam flux. The wire planes operate with Ar/CO_2 (90:10) at 1 atm. pressure. A chamber gas without hydrogen is important because the H(n,p) cross section is large and can contaminate the spectra especially at large angles where the hydrogen kinematics move the H(n,p) peak across the focal plane. All these innovations were utilized when the gas target box was designed.

After the proton exits the (n,p) target box it travels through the FECs and is momentum analyzed by the MRS.

3.4 MRS Electronics

There are two major parts to the MRS electronics, the trigger and the wire chamber readout. The trigger uses programmable LeCroy CAMAC crates that allows users to remotely change logic and delays for various inputs. The main trigger may be up to 6-fold logic. Included in the trigger is the front end trigger (FETRIG) which can incorporate up to four coincidence inputs e.g. from one of the planes of FEC∅. In CHARGEX running the signal from the veto scintillator is required to be absent for a valid event. Also included in the trigger are signals from the VDC X1 plane, the Focal Plane Polarimeter scintillators S1 and S2, and the focal plane paddles PD_{0-9}, all of which are required in coincidence with the signal from the front end trigger. The signal from the master trigger coincidence sets the latch which prevents any subsequent signals from altering the TDC and ADC values since the TDCs are operated in common stop mode. After the latch is set the computer reads the signals from the TDCs and the ADCs.

The MRS drift chambers are read out by a LeCroy drift chamber decoder system. Each wire from the FECs and VDCs is input directly to a LeCroy 4290 TDC in a special LeCroy crate which is controlled by a LeCroy 4298 module. The

signals from the wire planes in the segmented (n,p) target box are put through alternating routers which puts the signals alternately into one of two TDC channels. Since the TDCs are in common stop mode they have a high 'start' rate, so the routers are needed to reduce the inefficiency due to the TDCs (see section 4.3). For each trigger the electronics checks about 800 TDC channels. The 4298 module only passes data from the TDCs which fired. This information is passed to a LeCroy 4299 module which acts as a buffer. In normal MRS operation the computer reads the 4299 and clears the whole 4920 system when the MRS latch is cleared.

Chapter 4

A High Pressure Segmented Gas Target

4.1 Introduction

In order to study (n,p) reactions on gaseous isotopes it is necessary to have a suitable gas target. A segmented target for solids has been used at the TRIUMF charge exchange facility for some time [Hen+ 87], but recently a segmented high pressure gas target facility has been commissioned [Hen+ 89]. Certain constraints were placed on the design of this target. First of all it had to fit within the spatial constraints of the TRIUMF chargex facility and not reduce the maximum angle of the MRS. This restricts the total length to less than 17.5 cm and the use of a thin veto scintillator in front of the target restricts it by an additional 2 cm. Next, it had to hold gases at a high pressure to maximize target thickness, while not risking the loss of the target isotope. The backgrounds from the target box must also be small because they limit the smallest measurable cross sections. It was required that the target box have positions for solid targets to allow the simultaneous measurement of the spectra of solid targets of 'known' cross section. These are used to normalize the spectra of the gas targets. With such considerations the present target box was designed.

4.2 Target Box Design

Top and side views of the gas target are shown in figure 4.1. The target box was designed for use at 20 atm (294 psi). The gas target box is made of 7.9 mm stainless steel using welded construction with a gas flange on the top. The lid is made of 1" thick stainless steel and is sealed by an O-ring surface and attached to the rest of the box by 12 1/4"-28 high tensile steel bolts through the lid. The entrance and exit windows are 0.020" thick 602 stainless steel. All the components were designed to have a safety factor of two except for the lid bolts which have a safety factor of 12. The box has been leak tested up to 600 psi.

The segmented design allows different targets to be used. Each target layer is separated by a multi-wire proportional chamber (MWPC). This requires the target box to be filled with a counter gas to operate the wire chambers. To separate the target gas from the counter gas, the target gas is contained in separate cells inside the box with thin windows for isolation. The cells are removable and replaceable, as are the chambers. There are two different cell configurations, one uses one long cell, and the other uses two short cells separated by a detector layer. The two short cells are connected externally and are filled and vented together. The gas cell portion of the system was designed to maximize the amount of isotopic gas that actually contributes to the target volume. The total volumes of the two 4.0 cm long cells and of the single 9.3 cm long cell are $\simeq$153 cm^3 and $\simeq$180 cm^3 respectively. The volume of the tubing to the isotope cylinder is $\leq$10 cm^3.

The signal and high voltage leads from the wire chambers are fed through the lid of the box by connectors which are soldered on a piece of G-10 which is epoxied to the stainless steel lid. The wires are read out to preamplifiers which are mounted on the lid of the box. Each preamp consists of a diode-protected, common base input with low input impedance. The output uses two cascaded emitter followers. The preamps are mounted on the lid so that they are within 3 cm of the wire pads. The preamps then drive the output signals through 7 m of 50Ω miniature

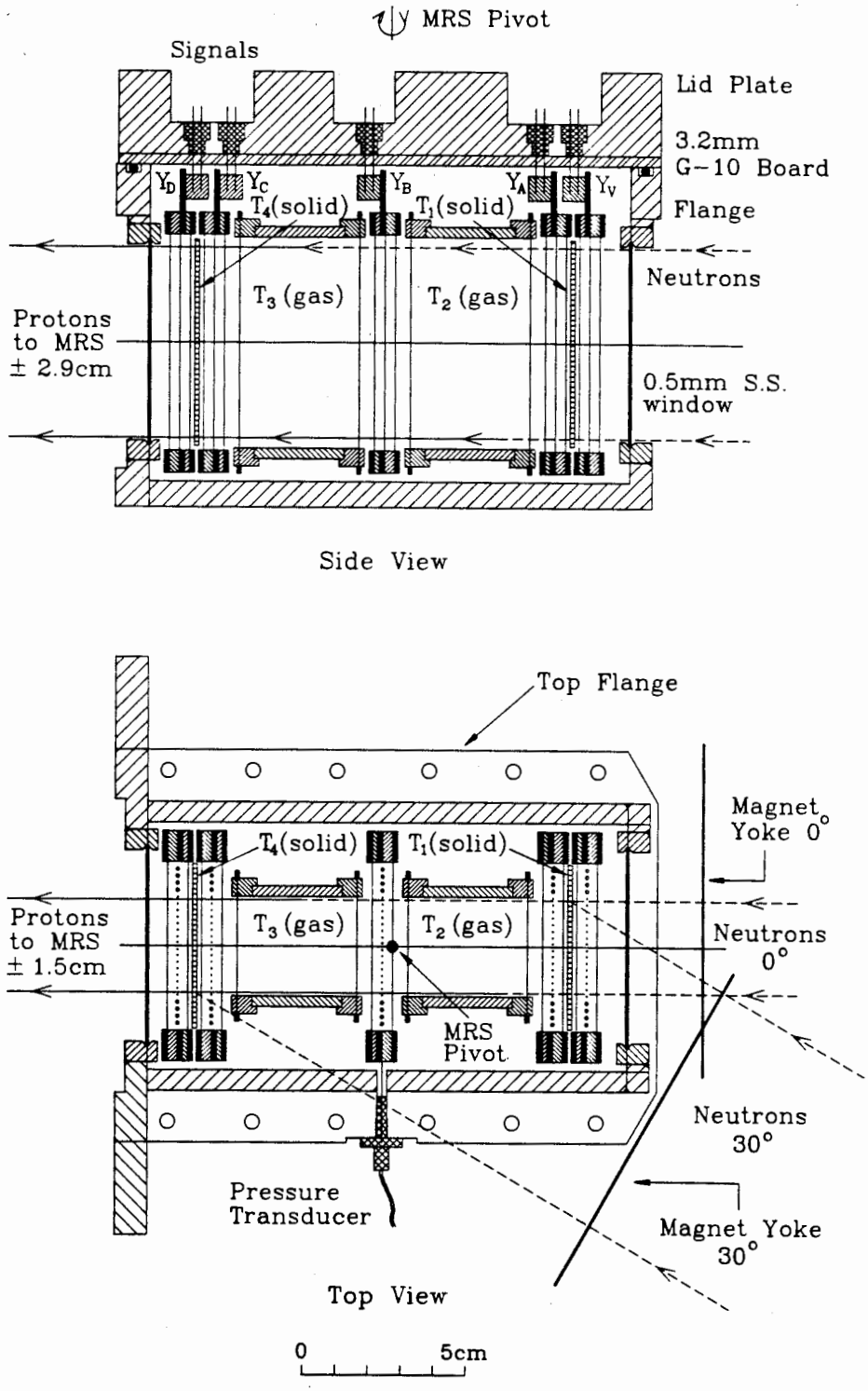

Figure 4.1: Side and top views of the segmented gas target box.

coaxial cable to LeCroy 2735 16-channel discriminator boards. The output of the discriminators is then fed into alternating routers developed at TRIUMF which puts the signal from each wire alternately to two different channels of a LeCroy 4291B 32-channel TDC. A schematic of the preamplifier circuit and a diagram of the read out electronics are shown in figure 4.2.

4.3 Detector Wire Chambers

The detector layers for the gas target are five MWPCs, Y_V, Y_A–Y_D. Y_V is a veto to protons that scattered into the target box or that converted from neutrons in the 0.020" stainless steel entrance window. Detectors Y_A to Y_D interleave the target layers to provide identification of the layer in which the (n,p) reaction occurred while allowing different targets to be used simultaneously. Energy loss corrections, ray-tracing and true scattering angle calculations also require knowing in which target layer the reaction took place.

Each wire chamber is made of one vertical wire plane sandwiched between two cathode foils. Each wire plane has 16-12 μm diameter gold-plated tungsten anode wires with a spacing of 2.0 mm. The cathode foils are made of 6.35 μm stretched aluminized mylar. The distance between the cathode foil and the wire plane is 3.18 mm. Each detector plane has an active area of 7.0 cm.(vertical) x 3.2 cm.(horizontal). The wires are read out in 8 pairs giving only horizontal spatial information with a resolution of about 4.0 mm. Table 4.1 summarizes the detector layer dimensions.

The target box wire chambers use a gas mixture of 90% Argon/10% CO_2. A gas mixture without hydrogen was used to reduce the background since the H(n,p) cross section is very large. Other mixtures, including ones of Ne/CO_2, were tested but found to break down at voltages far below attaining maximum efficiency. At 1 atm pressure the optimum efficiency was determined to be 1800 volts during bench tests. Since the gas box was to operate at 20 atm, the effects of high pressure on

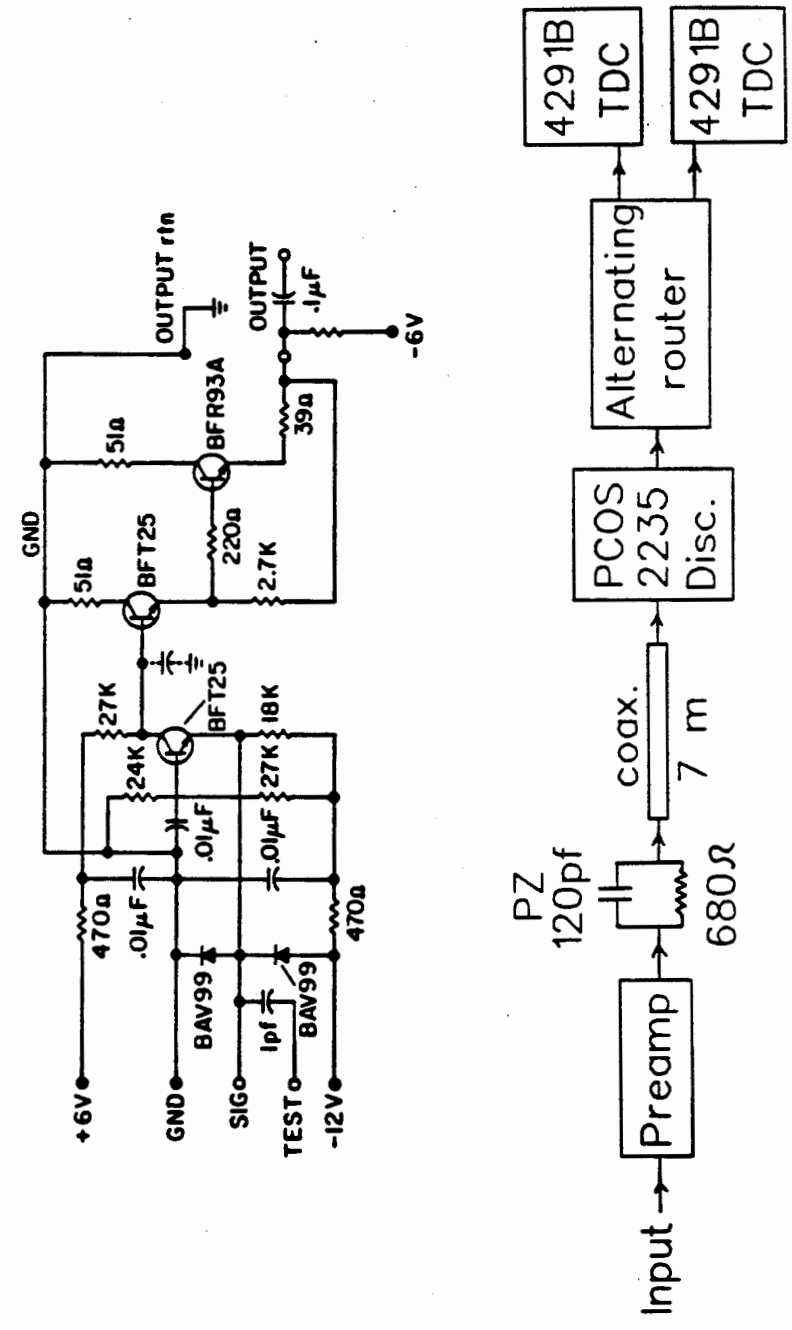

Figure 4.2: At the top is a schematic of the preamplifier circuit used to read out the wire chambers in the target box. The bottom diagram shows the chain of electronics for read out.

Table 4.1: Detector Layer Dimensions

Anode wire: 12 μm diameter gold-plated tungsten wire
Anode-anode distance: 2 mm
Cathode foils: 6.35 μm thick aluminized mylar
Wire-plane to cathode-plane distance: 3.18 mm
16 active anode wires, read out in 8 pairs
Spatial Resolution: 4 mm
Active area: 7.0(Vertical) x 3.2(Horizontal) cm^2

proportional chambers had to be determined. One effect of high pressure is seen in the gas gain. In a wire chamber gas gain depends on $V/\sqrt{P}$ where V is the voltage and P is the pressure. This means that if at 1 atm the optimum voltage is 1800 volts to get the same gas gain at 20 atm a voltage of 8049 volts would be required. Fortunately at the higher pressure twenty times more charge is also deposited so less gain is required. A voltage of 4900 volts gave an acceptable efficiency of $\geq$98% for protons.

Another effect of high pressure is seen in the collection of drift electrons. The electron drift velocity depends on the reduced electric field E/P where E is the electric field. The tails in the drift time spectra are associated with regions of small electric field and thus lower drift velocities. With the change from 1 to 20 atm the E/P decreases everywhere by a factor of 7.35, extending the regions of low electric field. This results in longer tails in the drift time spectra, even though the average drift time changes very little. Figure 4.3 shows the drift time spectra at 1 and 20 atm. Although the full width at half maximum (FWHM) are about 15 nsec at both pressures, the widths at tenth maximum (FWTM) are 29 and 33 nsec for 1 and 20 atm respectively. The broadening of the tail at 20 atm is only slight, and still quite acceptable.

The efficiency of the detector layers is important for many reasons. If there

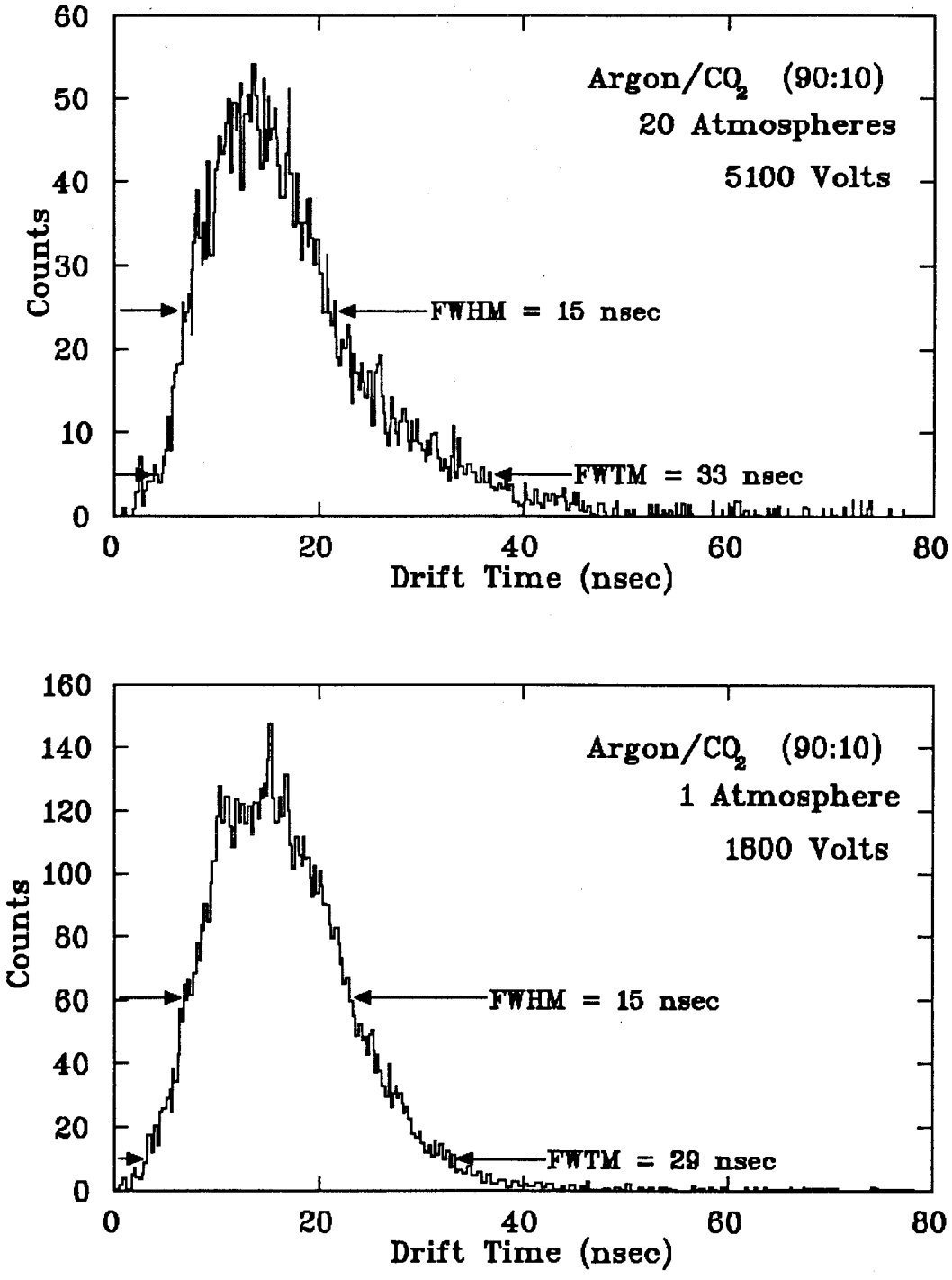

Figure 4.3: The drift time structures for the MWPCs at 20 atm (above) and 1 atm (below).

is an event in which a detector layer after the target layer in which the reaction occurred does not fire a hitpattern word is generated and the event is rejected. This results in fewer good events. This also results in the upstream targets having more rejected events than those downstream because there are more wire chambers after them that could fail to fire. This is corrected for in the analysis from the known product of the inefficiencies in the wire chambers that follow the target (see sec 5.3.1). If the missing detector is just after the target of the reaction it will result in incorrect target layer identification. This leads to the spectrum of the upstream target 'leaking' into the spectrum of the following target. It is also corrected for in the analysis.

There are two major sources of detector plane inefficiencies, one related to the pulse-pair resolution of the discriminators and one to the TDCs. The average pulse time over the discriminator threshold is ≈45 nsec and the discriminator reset time is ≈20 nsec. Then the pulse-pair resolution (T) for each channel should be ≈65 nsec. The efficiency is given by $\epsilon_{DISC} = e^{-CT}$ where C is the single events rate. During the experiment the singles rates were typically 150 kHz, which would give an inefficiency of about 1.0%. The other inefficiency is due to the effective deadtime of TDCs. The TDCs are operated in common-stop mode and have an effective dead-time (T) of about 200 nsec per pulse. If there were no routers, the efficiency would be related to the probability of two pulses occurring within the effective dead-time of the TDC's, given again by $\epsilon_{TDC} = e^{-CT}$, where C is the singles rate. For C=150 kHz the inefficiency would be about 3%. With the routers the efficiency of the TDCs depends on the probability of three pulses occurring within the effective dead-time (200 nsec) so $\epsilon_{TDC} = e^{-C^2T^2}$ giving an inefficiency of about 0.1%. Since the routers greatly reduce the TDC inefficiencies, the total inefficiency is dominated by the pulse-pair resolution in the discriminators. Typical inefficiencies measured during experiment were about 1.5% for running at 20 atm and about 0.8% for 1 atm.

4.4 Gas System

The gas target requires a complicated gas handling system. Firstly the isotopic targets are of a limited volume so the target must be filled and isolated. The isotope must also be recovered as a single volume. During the filling the difference in pressure between the chamber gas outside the cells and the isotope inside the cells must be kept low. After the cells are filled, chamber gas is flowed through the box to prevent the build-up and layering of gases which can poison the chamber gas and can degrade the wire chamber efficiency after long periods in the beam. With these considerations the present gas handling system was built. It consists of a series of manual valves on the inlet and outlet of the gas target box volume. There is also an electronic mass flowmeter on the inlet which allows the flow into the chamber volume to be controlled by signals from precise electronic pressure transducers. The gas system is shown in figure 4.4.

The features of the gas system are as follows:

- A premixed cylinder with a high pressure regulator supplies the chamber gas (Argon/CO_2 90:10) to the target box.
- A mass flowmeter with a full scale range of 2 litres/min regulates the gas flow into the target box. A Datametrics 825 mass flowmeter was used. This was controlled by a Datametrics 1511 flow controller and readout. The mass flowmeter can be adjusted for the different gases and flow ranges used. The controller box was operated in a mode which adjusts the flow with respect to a pre-set full scale range by comparing an input voltage to a 5.0 V full scale reference.
- The absolute pressure of the target box is monitored by a Kulite XT-190-500A miniature electronic pressure transducer which is mounted in the side of the target box. This has a rated absolute pressure range of 0–500 psi and a maximum pressure of 1000 psi. The differential pressure between the box

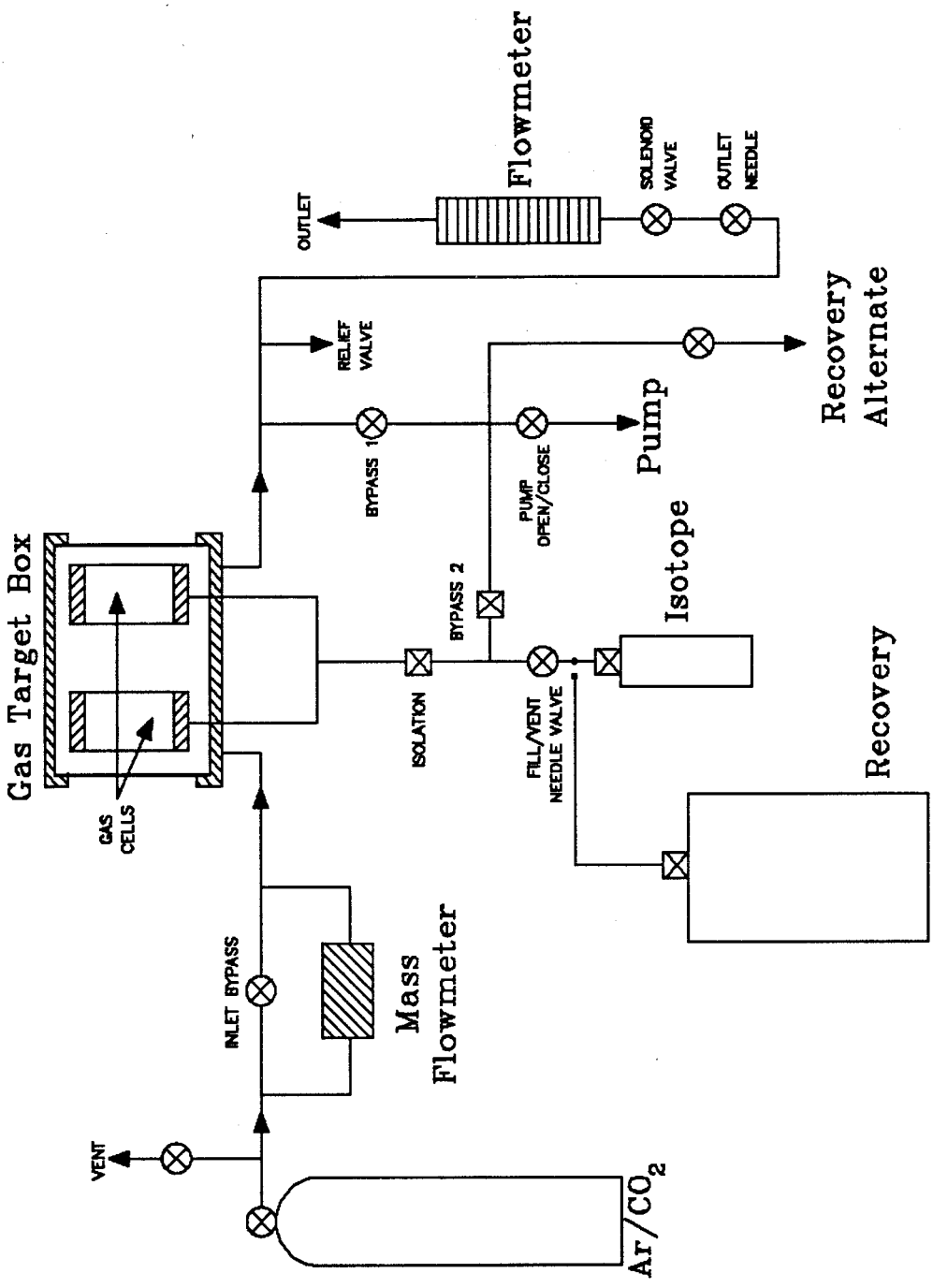

Figure 4.4: The gas system for the gas target box

and the cells is monitored by a Kulite XT-190-25D transducer mounted in the interface between gas fittings to the cells and a reference from the box. This transducer has a rated differential pressure of ±25 psi and a maximum pressure of ±50 psi. Each transducer requires a 10.0 VDC excitation voltage and gives an output of about 0–100 mV which is linear to the pressure. These were calibrated both at the factory and again at TRIUMF prior to installation and are linear to about 1.0 % of full scale.

- The pressure is controlled by refurbished MKS instruments 200/400 series PDR-5B pressure controller/readout. The readout has five channels which can be used as well as five set points which can be compared with the pressure signals. For our purposes a board with five amplifier circuits was installed in it. Two were used to amplify the outputs of the transducers to give a voltage that could be read out in units of pressure. One amplifier was used to compare the signals from the transducers to the reference voltages of the set points of the pressure controller/readout. This comparison was used to set the percentage of full scale flow set by the flow readout/controller. Far from the set point a maximum flow rate is set. Near the set point the flow and pressure difference have a steep linear dependence so if the pressure varies a little the flow changes rapidly. This is used to keep the pressure near the set point. If the pressure goes much beyond the set point the flow stops. The flow is usually controlled by the differential pressure but it can also be controlled by the absolute pressure. A 10 V DC power supply was also installed in the pressure controller/readout to power the transducers.
- Alarms are set by two of the unused set points. These detect if the differential pressure is too high or too low. If the differential pressure (P_{cell}-P_{box}) is too high another set point closes a solenoid valve which stops the flow out of the box. This solenoid valve also closes if power to the pressure readout/controller shuts off.

- A mechanical pressure relief valve is used to prevent over-pressuring the target box. It is set to open at 355 psi.
- The gas flow out of the target box is controlled by the outlet needle valve and monitored on a rotameter flowmeter.
- The gas cells are filled with isotopic target gas directly from a small volume (typically 75 to 320 cm^3) high pressure (typ. 1600 psi) cylinder, through the Fill/Vent (F/V) needle valve.
- Bypass valves allow the target box and the cells to be connected. The box and the cells can then be pumped out and filled either separately or as one common volume.
- The isotopic target gas is recovered into a large (typ. 50 litre) evacuated cylinder through the F/V needle valve.

4.4.1 The Filling Procedure

The filling procedure prevents excessive pressures across the cell windows, while filling the target reasonably quickly. The procedure takes about 25 min. The filling procedure is summarized as follows:

1. The mass flowmeter is turned off and the outlet needle closed, isolating the target box. The box and cells are connected through open bypass and isolation valves and are pumped out together.
2. The bypass valves are closed and, with the isolation valve open, the F/V needle is opened slowly, starting to fill the cells with the target gas. As the difference in pressure between the cells and the box increases, the controller/mass flowmeter adjusts the flow of Ar/CO_2 to the target box to maintain a constant differential. The F/V needle is adjusted during the fill to keep the mass flow at $\approx$1.5 litres/min (3/4 full scale).
3. When the operating pressure ($\approx$294 psi) is reached the cells are isolated and the outlet needle is adjusted until the flow rate is $\approx$150 cc/min.

4. The target gas remaining in the tubing outside the isolation valve may then be drawn into the recovery cylinder connected in parallel with the pump.

At all times, when filling and operating, a constant differential pressure ($\delta P \simeq 1.0$ psi) is kept to ensure a positive curvature of the cell windows. Loss of gas from the target cells has been quite small, typically about 5 cc (0.15%)/day. Over 4 days the pressure in the target cells may fall 2 psi. During that time the controller/mass flowmeter, by keeping the pressure differential constant, will have also reduced the target box pressure by 2 psi.

4.4.2 The Recovery Procedure

The technique for venting the target box and cells, while recovering the target gas, is as follows:

1. The recovery cylinder is connected to the F/V needle valve in place of the isotope cylinder. Bypass 2 is opened and the tubing from isolation valve to recovery cylinder pumped. Bypass 2 is then closed.
2. The outlet needle is adjusted to give a mass flow of typically 1.7 litres/min. The isolation valve is opened and the F/V needle gradually opened, starting the recovery of the target gas. As the difference in pressure between the cells and the box decreases the controller/mass flowmeter decreases the inlet flow of Ar/CO_2 to the box to maintain a constant differential pressure.
3. The F/V needle is adjusted during venting to keep the mass flow at $\approx$200 cc/min. The outlet needle is also adjusted to keep the outlet flow at $\approx$1.7 litres/min.
4. When the target box has been vented to atm pressure, the F/V needle is closed halting recovery. The outlet needle is then closed. The target box is pumped through Bypass 1 which is slowly opened.

5. As the pressure differential between the cells and the box increases the controller/mass flowmeter increases the inlet flow of Ar/CO_2 to the box to maintain a constant differential. Bypass 1 (needle valve) is adjusted until the inlet flow is 1.7 litres/min.
6. The F/V needle is again opened and adjusted to reduce the inlet flow to $\approx$200 cc/min. Finally, with the target box fully pumped, the inlet flow drops to zero and the F/V valve may be opened wide and the maximum target gas recovered.

Since the volume of the gas cell(s) plus tubing is $\simeq$163 cm^3 or $\simeq$190 cm^3 and of the recovery cylinder is 50 litres, most of the target gas in the cells may be recovered. The target gas is later transferred back to the original small volume cylinder using cryogenic techniques. An overall return of $\simeq$99% of the initial isotopic gas has been achieved.

If the target gas can be vented another procedure is used. Step 1 is followed as above. For step 2 the outlet valve is closed completely. Then bypass 2 is opened fully. Then bypass 1 is *slowly* opened which drops the pressure in the box. When bypass 1 is fully open the line between the box and the cells is fully pressurized. This means that the isolation valve can be opened. The cells and box are now bypasses and the inlet flow can be shut off and the outlet valve can be fully open, venting the cells and the chamber gas as a combined volume.

4.5 Instrumental Backgrounds

Backgrounds are a major concern in both for the design of the target and in the analysis of experiments. Backgrounds can limit the smallest measurable cross sections and can add major uncertainty to the results of any experiment if not properly understood. In the gas target box the backgrounds are due to (n,p) reactions on materials in the target box other than the target gas. There are two major sources of background; solids and gases.

The backgrounds due to solids are largely eliminated by the use of detector layers to reject conversions occurring outside the target cells. Thus the 0.020" thick entrance and exit windows are not a serious source of background since they are rejected by Y_V and Y_D respectively. The remaining sources of background from solids are: the cell windows, the wire chamber cathode foils and the anode wires. The cell windows are as thin as is mechanically usable. The first cell windows were made of .001" stainless steel (as used in E474) but these were later replaced by .0002" stainless steel to decrease the window-related background by a factor of five. At 0° the major contribution from this is due to the ^{56}Fe(n, p) Gamow-Teller peak (Q=–2.91 MeV). The cathode foils are made from aluminized mylar so the major background arises from the hydrogen with minor contributions from the carbon and oxygen. This could in principle be reduced by using thin aluminum foils which would eliminate all the hydrogen. The contribution from the anode wires is negligible since the wires are 12 μm thin and are spaced apart by 2 mm.

Gas contributions to the background are from the Ar/CO_2 mixture which is at the same high pressure as the target isotope. The active volume occupied by the Ar/CO_2 is minimized but at present the length of counter gas between the centers of the detector layers is about 25.3% of the total distance. The (n,p) reaction on Argon (99.6% ^{40}Ar) has a Q value of –6.721 MeV while the carbon (98.9% ^{12}C) (n,p) spectrum is well known with Q_{np} of –12.6 MeV and oxygen (99.8% ^{16}O) has a small cross section and Q_{np} of –9.64 MeV. The backgrounds can be adequately subtracted if the proper background runs are made. The contributions to the backgrounds are summarized in table 4.2

4.6 Target Options

The layered design of the gas target allows for simultaneous accumulation of data on two solid targets and two gas cells. The solid targets are placed in target positions A and D; between chambers Y_V and Y_A and Y_C and Y_D respectively.

Table 4.2: Materials associated with each of the target layers at 20 atm with ^{20}Ne target gas, and the .001" thick windows.

Material	Thickness		Hydrogen	Carbon
	(mg/cm^2)	(mm)	($\mu g/cm^2$)	(mg/cm^2)
EACH SOLID TARGET: T1, T4		3.1		
Argon/CO_2 90:10	34.4	9.5	0	1.02
EACH SHORT GAS CELL: T2, T3				
Argon/CO_2 90:10	50.0	13.9	0	1.49
Neon-20	70.9	39.7		
Stainless steel foils	20.1	$2.5x10^{-2}$		
OR				
THE LONG GAS CELL: T2A				
Argon/CO_2 90:10	50.0	13.9	0	1.49
Neon-20	167	93.3		
Stainless steel foils	20.1	$2.5x10^{-2}$		
FOR EACH TARGET:				
MWPC Al-mylar foils	1.67	$1.37x10^{-2}$	69.4	1.11

There is space for targets of thickness $\leq$3.1 mm. The targets used should include at least one CH_2 in the last target position to allow normalization to the absolute cross section of H(n,p). The CH_2 also allows the extraction of the incident neutron spectrum. A carbon target in the first position might also be used to allow the subtraction of the carbon contribution to the CH_2 spectrum. Possible gas targets include non-corrosive isotopes of interest from ^3He to ^{130}Xe. For good statistics the long cell is used. The two small gas cells are used if good resolution is required. Normalization can be done directly for the gas cells by doing a run with methane or H_2 in them. Background runs are done with Ar/CO_2 at 1 and 20 atm.

In E474 the target stack consisted of solid targets of 44.4 mg/cm^2 of CH_2 in

positions A and D. The two short cells were filled with 20 atm of 99.98% enriched ^{20}Ne for a total gas target thickness of 145 mg/cm^2. At each angle three runs were done; one for the ^{20}Ne target at 20 atm and one for Ar/CO_2 each at 20 atm and 1 atm. The ^{20}Ne target was 99.98% enriched.

Chapter 5

Data Analysis

5.1 Data Stream from the MRS

The computer reads the CAMAC TDC and ADC values in an order specified by an event processor file in the TWOTRAN language. A typical data stream from the MRS for (n,p) mode CHARGEX running consists of:

- three header words consisting of event length, event type, and a sequence number.
- a Digital Coincidence Register (DCR) word and a termination code.
- 8 TDC signals which are used to define timing from the scintillators and then a termination code.
- 12 ADC signals which give the energies in the various scintillators and a termination code.
- 3 ADC signals from the two large FPP scintillators and a termination code.
- two VDC header words and two words (wire number and TDC value) for each of the drift chamber wire TDCs which did not time out making a variable length word including up to 110 channels.

5.2 LISA

The data stream is analyzed by the LISA data analysis program. LISA does event by event analysis both on-line or during replay. The analysis of each event has two parts. First the TDC values from the struck wires are decoded into position coordinates in each wire plane by the DRIFT routine. Then these coordinates are used in the INSERT routine to do ray-tracing and event reconstruction. The DRIFT and INSERT routines can easily be changed by the user according to the needs of different experiments. From these routines the basic spectra are created and corrected for both kinematics and optical aberrations on an event by event basis.

5.2.1 Wire Chamber Decoding

The wire chamber decoding is done by the DRIFT routine which gets the wire number and drift time values from the TDCs for each event and transforms them into position coordinates. The details of this are in the MRS manual [MRS]. Since the TDCs are operated in common stop mode, small TDC values correspond to long drift times.

The DRIFT routine also does crude ray-tracing to the segmented target. To reduce the target misidentification due to accidental coincidences in the target box MWPCs, only wires in the vicinity of the traced back position are considered in defining a particular event. The traced back position is somewhat smeared out by multiple scattering of the proton in the 0.020" exit window. This effect is seen in figure 5.1 which shows the calculated versus the (calculated – measured) horizontal positions in wire chambers Y_A and Y_D. It is largest for the first two detector layers Y_V and Y_A. For these detectors the four closest pairs of wires to the traced back position are used while only the two closest are used for Y_B, Y_C, and Y_D. In figure 5.1 the eight channels which are read out are clearly visible in the plot. The horizontal band at –4.0 mm corresponds to events in which that wire

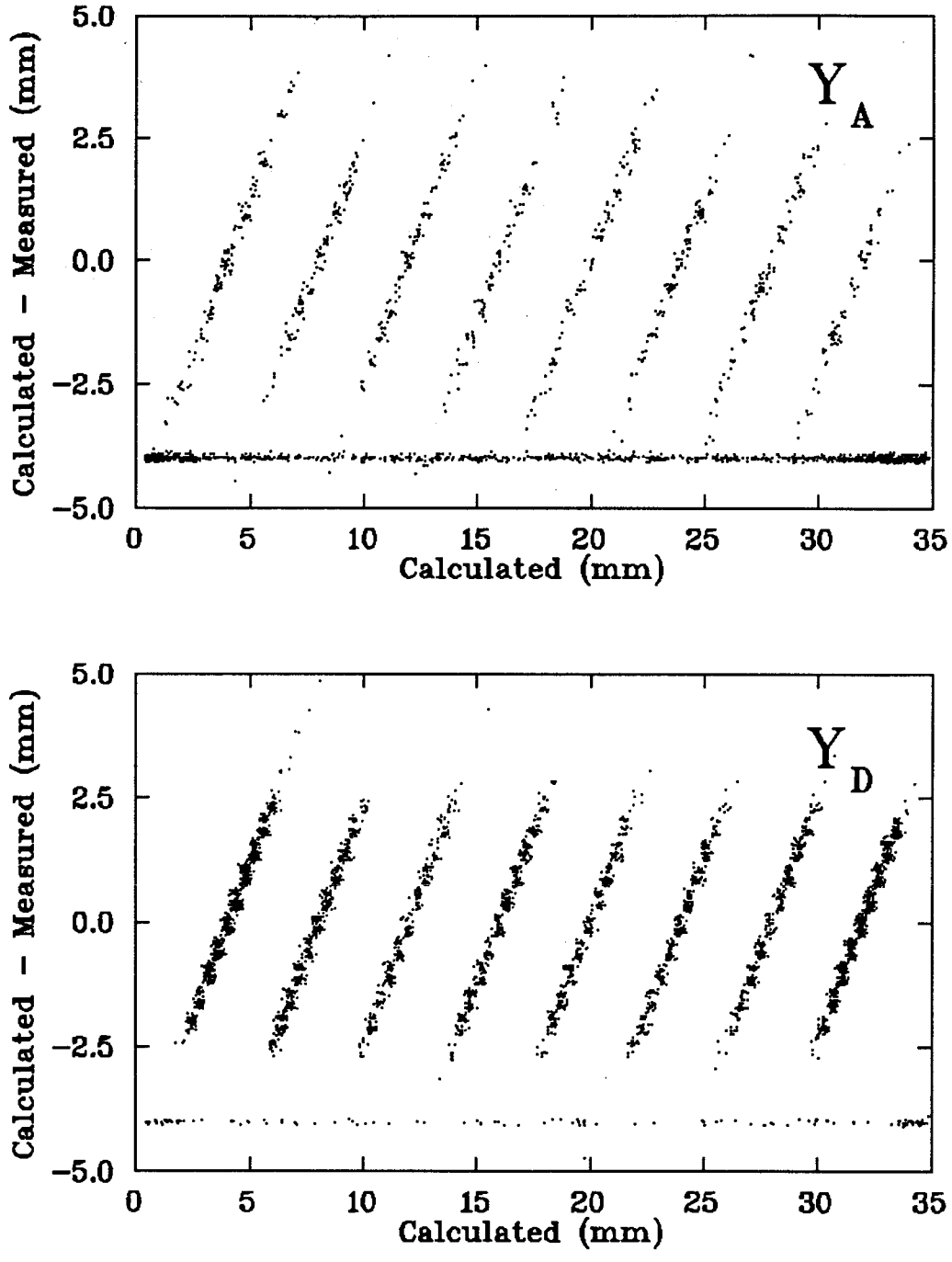

Figure 5.1: Plot of the calculated horizontal position versus the (calculated − measured) positions for wire planes Y_A and Y_D. The eight channels which are read out are clearly visible. The horizontal band at −4.0 mm corresponds to events in which that wire plane did not register even though there was a trigger in the MRS.

plane did not register even though there was a trigger in the MRS. This comes mainly from neutrons which did not convert before the particular chamber but converted later. This explains why this band is larger and why there are fewer good events in the upstream detector, Y_A.

5.2.2 Target Coordinate Reconstruction

Target coordinate reconstruction is done by the FECs and the target detector planes identify the target. Figure 5.2 shows the coordinates involved in the calculation. The scattering angle in the X direction is:

$$\theta_{\mathrm{FEC}} = \frac{\mathrm{X}\emptyset - \mathrm{XM}}{\mathrm{d_{FEC}}} \tag{5.1}$$

where $\mathrm{d_{FEC}}$ is the distance between FECM and FEC$\emptyset$. The scattering angle in the Y direction is:

$$\phi_{\mathrm{FEC}} = \frac{\mathrm{Y}\emptyset - \mathrm{YM}}{\mathrm{d_{FEC}}} \tag{5.2}$$

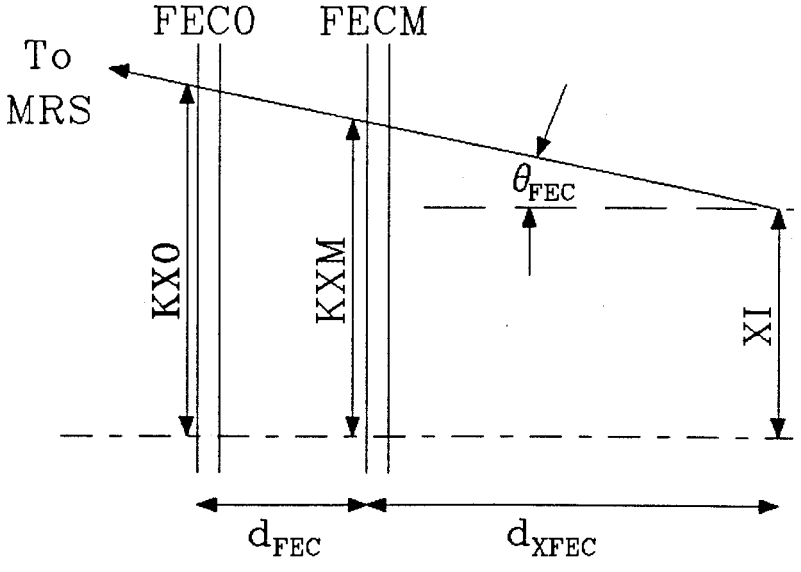

Figure 5.2: Target coordinate reconstruction from FECM and FEC$\emptyset$.

The target position can then be calculated as follows:

$$\mathrm{XI} = \mathrm{XM} - \mathrm{d_{XFEC}} * \theta_{\mathrm{FEC}} \tag{5.3}$$

$$\mathrm{YI} = \mathrm{YM} - \mathrm{d_{YFEC}} * \phi_{\mathrm{FEC}} \tag{5.4}$$

where d_{XFEC} and d_{YFEC} are the distances from the target center to XM and YM respectively and depends on which target the reaction took place in. Software cuts are made on the target coordinates to reject reactions which took place in the gas cell walls.

The FECs are also used to calculate the true scattering angle of the particle. The angle of the incoming neutron is defined by the angle from the center of the (p,n) target where the proton beam is focused to the position in the target of the (n,p) reaction which is given by XI, YI from above and the 'Z' from the target identification. The angle of the outgoing proton is defined by θ_{FEC} and ϕ_{FEC} above. The true scattering angle is then defined as the difference in angle between the incoming and outgoing particles.

5.2.3 Focal Plane Coordinate Reconstruction

The momentum of the protons analyzed by the VDCs at the focal plane of the X1 and X2 is used to calculate the position of the outgoing particle along the bend plane. The bend plane coordinate 'XF' measures the momenta of the particles. Figure 5.3 shows the coordinates involved in the calculation. XF is calculated as,

$$\mathrm{XF} = \frac{(\mathrm{VDCDIST} \cdot \mathrm{X1C}) - (\mathrm{FOCALF} \cdot \mathrm{DX12})}{\mathrm{VDCDIST} - (\mathrm{DX12}) \cdot \tan\delta)} \tag{5.5}$$

where VDCDIST is the distance between the VDCs, FOCALF is the distance between VDC1 and the true focal plane. DX12 is the difference between the corrected value of X1 (X1C) and the value of X2 and δ is the angle between the X-plane of the true focal plane and the X-plane of the VDCs.

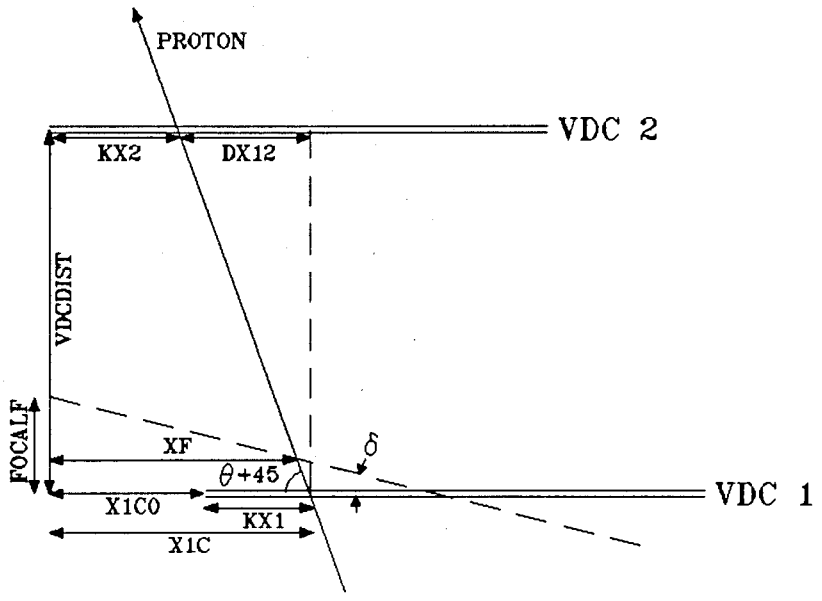

Figure 5.3: Focal plane reconstruction from VDCs.

After the focal plane spectrum is calculated it is corrected with respect to the bend plane angle, θ. It is also corrected for aberrations in the focal plane, making XF independent of scattering angles (θ_{FEC}, ϕ_{FEC}) and target position (XI and YI) by adding linear and quadratic correction terms. The kinematics are corrected for by making XF independent of the true scattering angle again using linear and quadratic correction terms. The aberration corrections are found empirically at 0° and used throughout the analysis while the kinematic corrections are calculated for each angle.

5.3 Corrections to Spectra

After obtaining the raw spectra from the data replay the spectra must also be corrected for backgrounds etc. A standard set of corrections is used for both segmented (n,p) target boxes with some modifications for the different backgrounds

of the gas target box. The corrections made are as follows:

5.3.1 Wire Chamber Inefficiencies

The efficiencies of the wire planes in the target box are measured during the experiment by positioning a thick CH_2 in the neutron beam upstream of the target and requiring a hit in the veto scintillator in the trigger. This means that the neutrons convert in the CH_2 and a proton beam traverses all the wire chambers in the target box. The efficiencies of each wire plane in the box can then be determined from a spectrum of missing hits. The efficiencies are on the order of 99% for single detector plane misses.

The wire chamber inefficiencies have two effects on the spectra. First, if a wire chamber misses when an upstream chamber fires the event is rejected in software. This means that the upstream targets have fewer counts because there are more downstream chambers which have the possibility of not firing. Each target spectrum must therefore be corrected to account for missing hits in any of the wire chambers further downstream. This can be done by multiplying each spectrum by the inverse of the product of the efficiencies of all the downstream chambers. This correction is about 10% for the first target.

The second effect of wire plane inefficiencies is that if the wire chamber directly following the hit target misses but all the others downstream fire it is counted as a good event but the target is misidentified. This means that the spectrum from one target is contaminated by the spectrum from the upstream target on the order of the inefficiency of the upstream detector. This is corrected for simply by multiplying the upstream spectrum by the inefficiency of the chamber directly following it and subtracting the product from the spectrum of the target immediately downstream. This contamination can be large if the upstream target has a much larger cross section than the downstream target or if chamber efficiencies are low. In E474 the first target was 44.4 mg/cm^2 CH_2, while the second target was ^{20}Ne

so the leak through of the hydrogen peak into the ^{20}Ne spectrum was significant. If the first target has a small yield the leak through of the front stainless steel window might have to be corrected for.

The corrections to the spectra were made as follows. If wire planes (i=A-D) have inefficiencies η_i, and efficiencies $\epsilon_i = 1 - \eta_i$, the total efficiency of all wire planes A–D is

$$\epsilon_{\rm A}^{\rm TOT} = (1-\eta_{\rm A})(1-\eta_{\rm B})(1-\eta_{\rm C})(1-\eta_{\rm D})$$

and for downstream targets,

$$\epsilon_B^{TOT} = (1-\eta_B)(1-\eta_C)(1-\eta_D)$$

$$\epsilon_C^{TOT} = (1-\eta_C)(1-\eta_D)$$

$$\epsilon_D^{TOT} = (1-\eta_D)$$

The corrected spectra are related to the raw spectra as follows;

$$A^C = 1/\epsilon_A^{TOT} \cdot A^{RAW}$$

$$B^C = 1/\epsilon_B^{TOT} \cdot B^{RAW} - \eta_A \cdot A^C$$

$$C^C = 1/\epsilon_C^{TOT} \cdot C^{RAW} - \eta_B \cdot B^C - \eta_A \cdot \eta_B \cdot A^C$$

$$D^C = 1/\epsilon_D^{TOT} \cdot D^{RAW} - \eta_C \cdot C^C - \eta_B \cdot \eta_C \cdot B^C - \eta_A \cdot \eta_B \cdot \eta_C \cdot A^C$$

where i^{RAW} are spectra before inefficiency correction and i^C are the corrected spectra. Usually corrections involving terms with the product of two or more inefficiencies can be ignored.

5.3.2 MRS Acceptance

The MRS has a finite acceptance which varies as a function of the focal plane position. This function can be measured by varying the field settings of the dipole magnet to move the hydrogen peak from a CH_2 target across the focal plane. The total counts in this peak are then compared to the total beam integration for each magnet setting and normalized. Then the points are fitted to a polynomial to obtain an acceptance function. For E474 time constraints did not allow for the acceptance to be measured, so the acceptance function was obtained from the

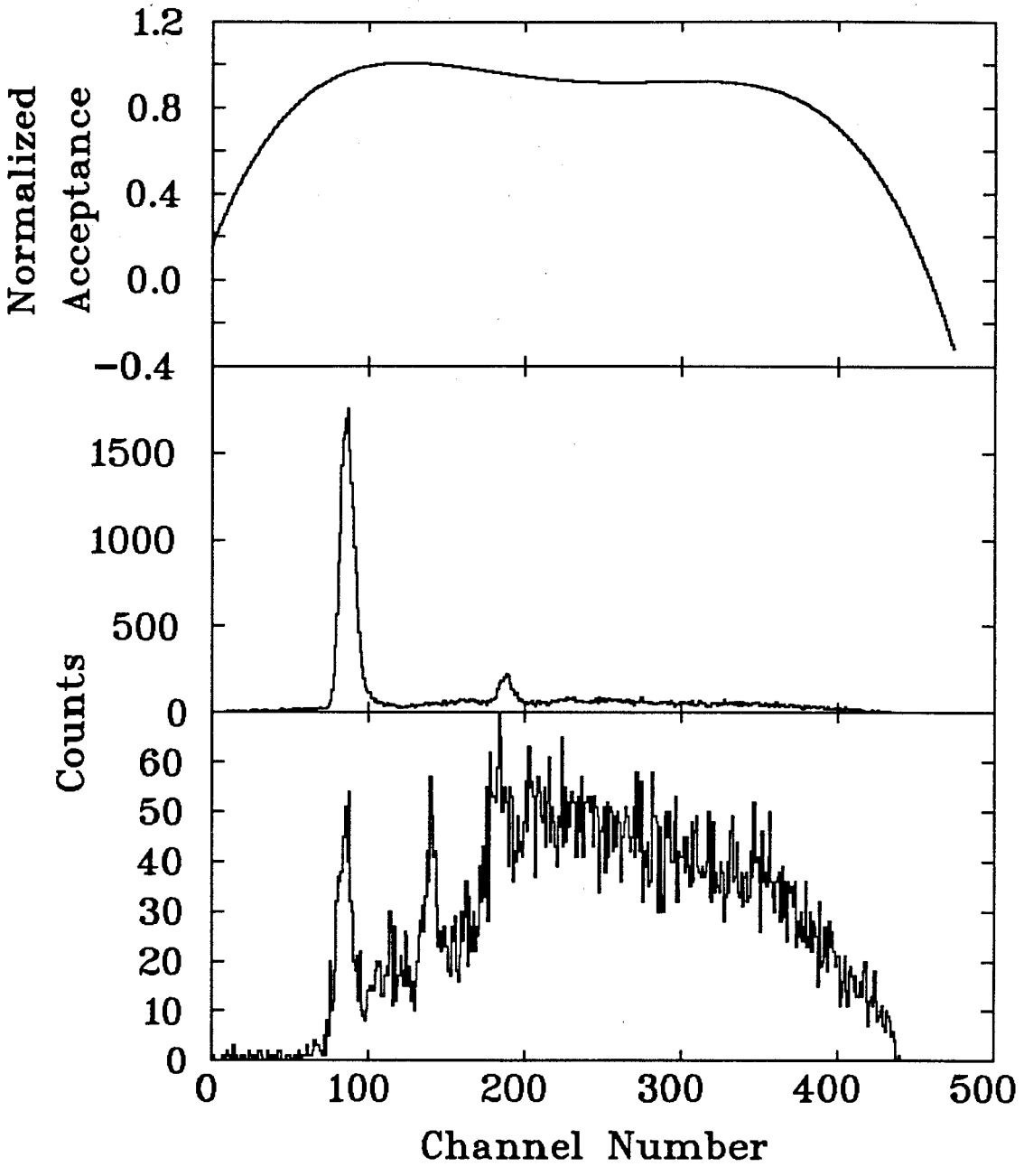

Figure 5.4: The acceptance function from E489 (top) and the CH_2 (middle) and ^{20}Ne (bottom) spectra before acceptance correction.

analysis of E489 which was at the same energy. To correct for acceptance each spectrum is divided by the acceptance function. The acceptance is most important in the high excitation end of the spectrum. Figure 5.4 shows the normalized acceptance function from E489 (top) with the uncorrected spectra of CH_2 (middle) and ^{20}Ne (bottom) to show the spectra relative to the acceptance.

The acceptance and neutron flux are somewhat target dependent, but since the dependence is roughly linear the symmetry of targets (CH_2-^{20}Ne -^{20}Ne -CH_2) should eliminate any effect. At high MRS angles the drop in the cross section of the $^7Li(p,n)$ reaction decreases the neutron flux at the extreme targets. The effects of this are minimal in the present experiment but it is important at MRS angles $\geq 15°$.

5.3.3 Energy Loss Corrections

Before the spectra from like targets can be summed the spectra have to be shifted with respect to each other to correct for the energy loss in each target. Energy losses can be calculated but the shifts are found better empirically. Once these shifts are made the spectra for like targets are summed. For E474 targets A and D are both CH_2 and are summed. Targets B and C are both ^{20}Ne or Ar/CO_2 and are therefore summed for each target.

After the energy loss correction is done the 1 atm background spectra must be artificially broadened so the resolution of the peaks is the same as that of the 20 atm runs. This is needed because at 1 atm there is less target material in the cells so the peaks are significantly narrower. This broadening ensures a reasonable subtraction of background peaks.

5.3.4 Background Subtraction

After all the spectra are corrected for wire chamber efficiency, MRS acceptance and energy loss the backgrounds have to be subtracted. The different runs must first be normalized to the same integrated beam current. This is done by integrating

the H(n,p) peaks of the CH_2 spectra of the two background runs and normalizing to counts in the H(n,p) peak of the ^{20}Ne run for each angle.

The measured spectra contain contributions from the target of interest in the cells as well as backgrounds from Ar/CO_2 chamber gas outside the cells at the same pressure and solids in the detectors and cell windows. The measured spectrum of ^{20}Ne at 20 atm. ('NE20') contains:

$$^{20}Ne \text{ @ 20 atm. } + \text{ } Ar/CO_2 \text{ bkgd @ 20 atm. } + \text{ solids bkgd} \tag{5.6}$$

The measured spectrum of Ar/CO_2 at 20 atm. ('AR20') contains:

$$Ar/CO_2 \text{ @ 20 atm. } + \text{ } Ar/CO_2 \text{ bkgd @ 20 atm. } + \text{ solids bkgd} \tag{5.7}$$

The measured spectrum of Ar/CO_2 at 1 atm. ('AR1') contains:

$$Ar/CO_2 \text{ @ 1 atm. } + \text{ } Ar/CO_2 \text{ bkgd @ 1 atm. } + \text{ solids bkgd} \tag{5.8}$$

The backgrounds are subtracted as follows:

- **Subtract (3) from (2) i.e.:**

$$\text{AR20} - \text{AR1} = \text{AR19} = Ar/CO_2 \text{ @ 19 atm. } + Ar/CO_2 \text{ bkgd @ 19 atm.} \tag{5.9}$$

- **Normalize (4)·20/19:**

$$\text{AR19} \cdot 20/19 = \text{AR} = Ar/CO_2 \text{ @ 20 atm. } + Ar/CO_2 \text{ bkgd @ 20 atm.} \tag{5.10}$$

- **Extract solid background (2)-(5):**

$$\text{AR20} - \text{AR} = \text{SOLID} = \text{ solid bkgd} \tag{5.11}$$

- **Normalize (4)·20/19 · 0.253 to extract Ar/CO_2 background:**

$$\text{AR19} \cdot 20/19 \cdot 0.253 = \text{ARBKGD} = Ar/CO_2 \text{ bkgd @ 20 atm.} \tag{5.12}$$

- **Extract pure ^{20}Ne spectrum (1)-(6)-(7)=(8):**

$$\text{NE20} - \text{SOLID} - \text{ARBKGD} = \text{NEON} = {}^{20}\text{Ne @ 20 atm.} \quad (5.13)$$

This yields the ^{20}Ne spectrum with the gas and solid backgrounds subtracted. The factor of 0.253 in (5.12) is the ratio of the length of gas volume *outside* the gas cells to the total length of the gas volume (the distance between the detector planes).

Figure 5.5 shows the results of the background subtraction. The top figure shows the ^{20}Ne spectrum before the background subtraction. The second spectrum is the background from solids. The contributions from the H, ^{12}C, ^{56}Fe (n,p) spectra are clearly seen. The third spectrum is the background due to the Ar/CO_2 chamber gas with the ^{12}C(n,p) peak visible. The last spectrum is the background subtracted ^{20}Ne spectrum 'NEON' normalized to cross section but without any other corrections. Peak at Q=0 MeV is due to the hydrogen which is not completely subtracted.

5.3.5 Deconvolution of Neutron Spectrum

The neutron beam is not perfectly monoenergetic but has finite width and a tail. This tail has to be deconvoluted and the neutron source be treated as monoenergetic for a good interpretation of the spectra. The shape of the neutron spectrum can be found by subtracting a normalized ^{12}C(n,p) spectrum from the CH_2(n,p) spectrum. This yields the shape of the H(n,p) spectrum which reflects the shape of the neutron spectrum. The neutron spectrum is used to deconvolute the ^{20}Ne(n,p) spectrum by finding the contributions to the total neutron flux from the peak and from the tail. The contribution from outside the neutron peak is stripped away. This is done with a computer code. Figure 5.6 shows the neutron spectrum with both linear and log scales (top and upper middle) and the unstripped (lower middle) and the stripped ^{20}Ne spectrum (bottom).

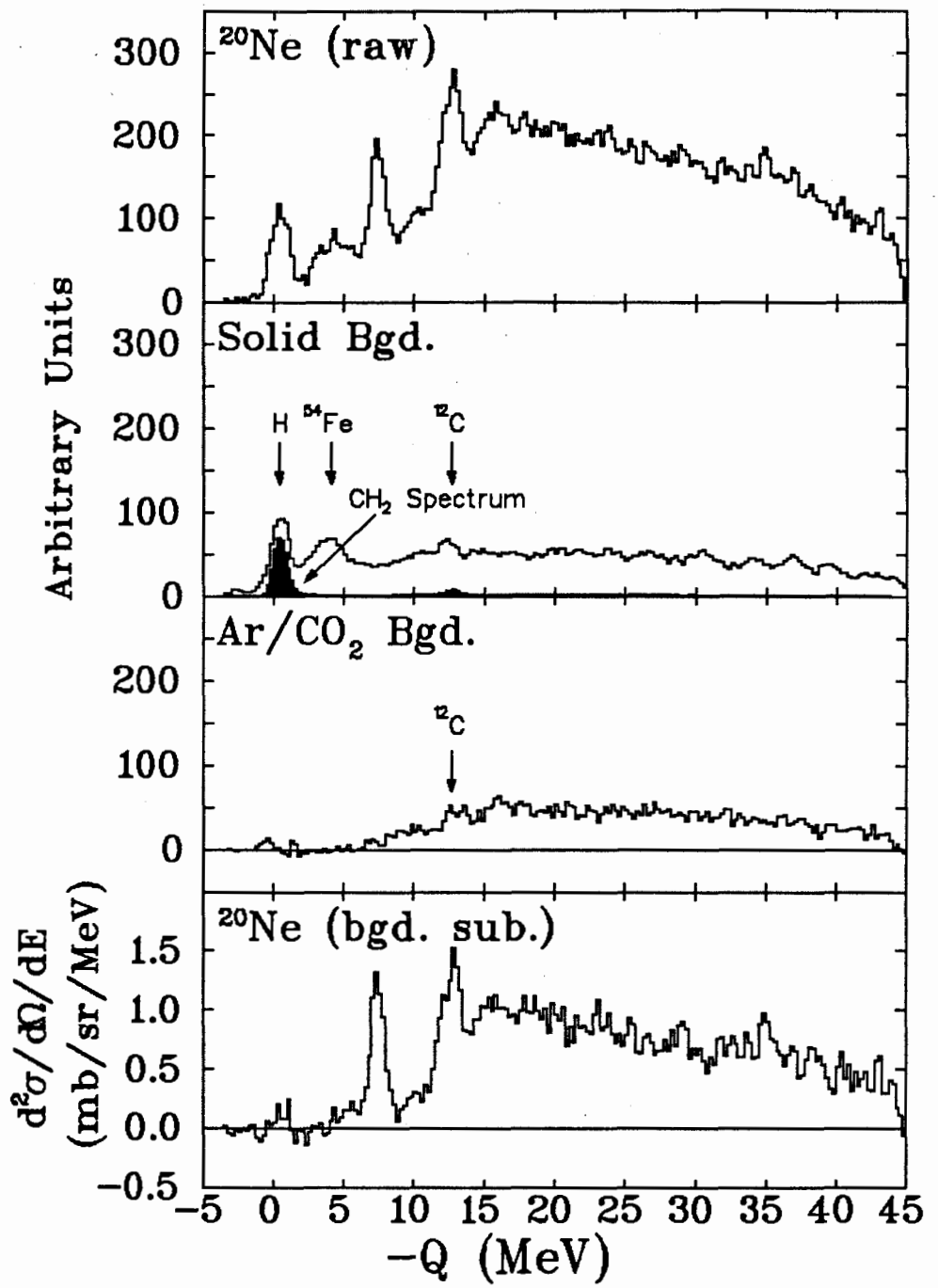

Figure 5.5: The ^{20}Ne(n, p)^{20}F spectrum at E_n = 198 MeV at θ_{lab}=1.52° showing the various contributions to the background. The top spectrum shows the ^{20}Ne before background subtraction. The next two spectra show the backgrounds due to solids and chamber gas. The bottom spectrum is of ^{20}Ne with the backgrounds subtracted and normalized to units of cross section.

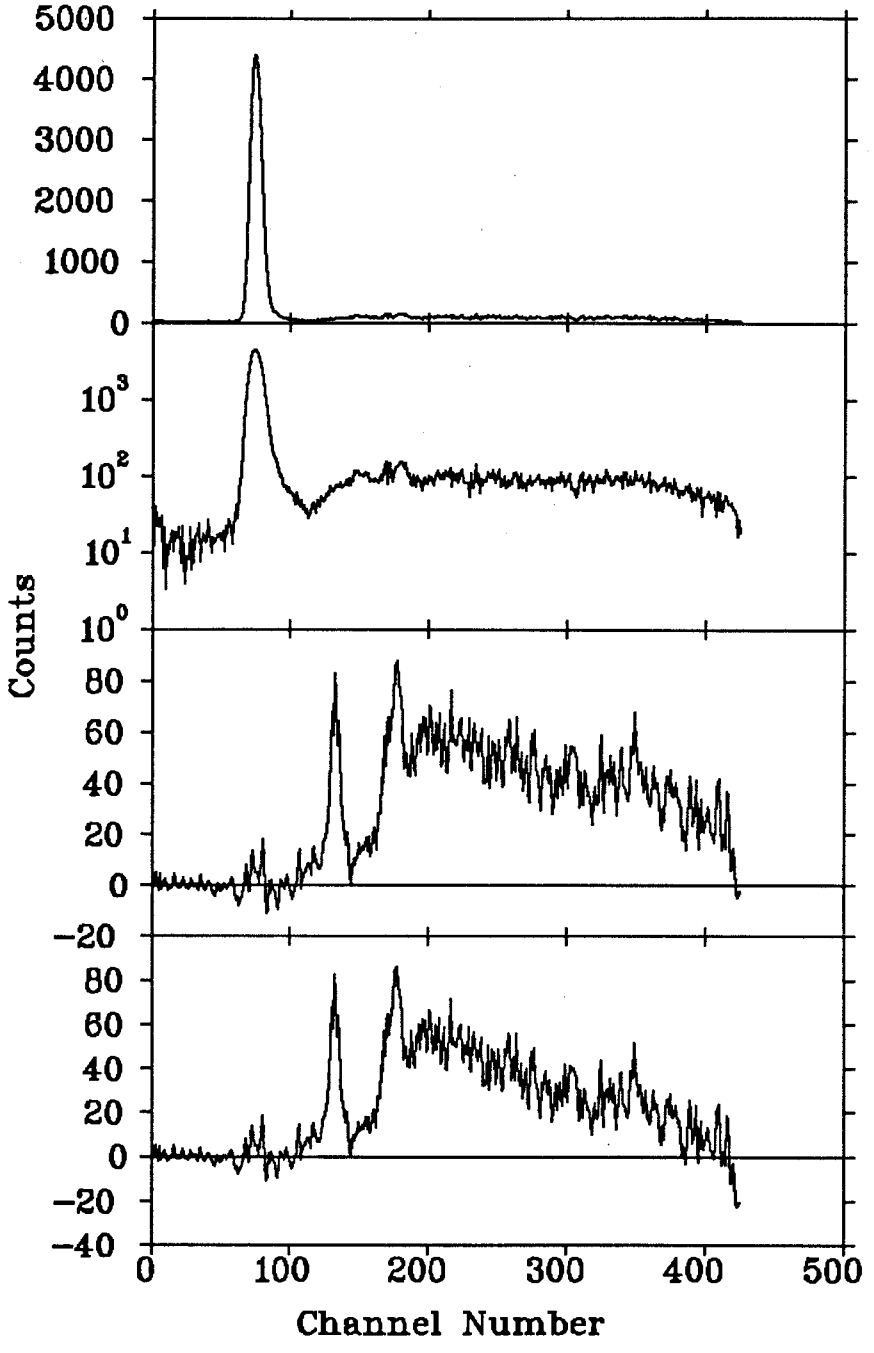

Figure 5.6: The neutron spectrum with both linear and log scales (top and upper middle) and the unstripped (lower middle) and the stripped ^{20}Ne spectrum (bottom).

5.3.6 Rebinning of Spectra

After the neutron tail is stripped away the resulting spectrum is rebinned in a desirable bin size which optimizes statistics against resolution. Since the resolution of the major peaks in the ^{20}Ne spectrum was found to be about 1200 keV a bin size of 0.5 MeV is reasonable, but for the multipole decomposition a bin size of 1.0 MeV was used.

The spectra are rebinned into units of energy, calibrated in terms of excitation energy. Since the original focal plane coordinate, 'XF', is a momentum, the conversion to energy requires finding the dispersion with both linear and quadratic terms. The dispersion can be found by measuring the centroids of peaks of known excitation energy, (e.g. in the ^{12}C(n,p) spectrum) and fitting the coordinates to the energy or from comparing the position to the field settings from the acceptance measurements. For E474 the dispersion was found by both methods, indirectly for the first method. They gave approximately the same result. The excitation energy is known to about $\pm$200 keV.

Finally, the spectra are divided by bin size to yield the normalized double differential cross section $d^2\sigma/dE/d\Omega$. The absolute values of the cross sections are determined below.

5.3.7 Calibration of Spectra

Cross sections for the target gas are determined relative to simultaneously measured spectra of solid targets with 'known' cross section. For E474 targets A and D were CH_2 so as to use the 'known' cross section of the H(n,p) reaction. In general, the yield for a specific reaction is given by,

$$Y = I \cdot \frac{d\sigma}{d\Omega} \cdot d\Omega \cdot n \cdot x \tag{5.14}$$

where Y is the yield, I is the beam current, n is the number density of target atoms in number per cm^3, x is the target length in cm and $d\Omega$ is the acceptance of

the spectrometer. The product is $n \cdot x = \tau \cdot N_A/m$ where τ is the target thickness in mg/cm^2 and is found by assuming the gas is an ideal gas and measuring the pressure and volume. Also N_A is Avogadro's number, and m is the molar mass of the target atoms. The ratio of ^{20}Ne yield to H yield is then:

$$\frac{Y_{Ne}}{Y_H} = \frac{(I \cdot \tau \cdot N_A/m \cdot \frac{d\sigma}{d\Omega} \cdot d\Omega)_{Ne}}{(I \cdot \tau \cdot N_A/m \cdot \frac{d\sigma}{d\Omega} \cdot d\Omega)_H} \tag{5.15}$$

For simultaneous accumulation $I_{Ne} = I_H$, N_A is a constant and $d\Omega_{Ne} = d\Omega_H$, i.e.

$$(\frac{d\sigma}{d\Omega})_{Ne} = (\frac{d\sigma}{d\Omega})_H \cdot \frac{Y_{Ne} \cdot m_{Ne}}{Y_H \cdot m_H} \cdot \frac{\tau_H}{\tau_{Ne}} = \alpha \cdot Y_{Ne} \tag{5.16}$$

The H(n,p) cross sections are obtained from the Arndt phase-shifts fit SAID at that center of mass true scattering angles and reconverted to lab angle cross sections [AS 84]. Then the proportionality between counts in the hydrogen peak and the cross section is found. The integral of the hydrogen peak then gives the normalization constant 'α' to convert counts in the ^{20}Ne spectrum to cross sections. The results are shown in table 5.1. From this each spectra is calibrated in terms of laboratory cross section. The spectra are then converted to center of mass cross sections by calculating the theoretical ratio of lab to cm at different energy bins. This is necessary for comparison with theory.

Table 5.1: H(n,p) cross sections and calibration constants 'α'

θ_{lab}	θ_{cm}	σ_{lab}(H(n,p)) (mb/sr)	Y_H (counts)	α (mb/sr/count)
1.53	1.63	53.53	44874±211	.00218±.00023
3.34	3.54	48.20	24064±155	.00348±.00036
6.30	6.68	40.18	33540±188	.00219±.00026
10.11	10.72	31.28	8429±94	.00634±.00071
15.3	16.22	24.56	5717±80	.00729±.00094

The errors are found at each step of the analysis and are taken through each

part of the calculation. The error begins with the statistical error in the raw spectra and the uncertainties introduced by different parts of the data analysis are added in. The result is an error assigned to each bin of data in each spectrum.

Chapter 6

Results

The final $^{20}Ne(n,p)^{20}F$ spectra at five angles in 0.5 MeV bins are shown in figure 6.1. The spectra show two major peaks, one at 1.0±0.3 MeV and the other at 6.5±0.5 MeV, with only hints of other structure. With the resolution being 1.2 MeV FWHM individual states cannot be resolved. The angular distribution of the spectra suggests that these peaks both have contributions from $\Delta L=0$ and $\Delta L=1$ transitions. The peak at 6.5 MeV is superimposed on a large background making it impossible to isolate and examine its angular distribution. The peak at 1.0 MeV is clean enough to measure its cross section at different angles so a decomposition was done by fitting its angular distribution to theory. A full multipole decomposition was done on the total spectrum separately.

6.1 Multipole Decomposition

6.1.1 The 1.0 MeV Peak

The cross sections of the 1.0 MeV peak were found by fitting the peak by a skewed gaussian distribution assuming no background. The fits are reasonable at θ_{lab}=1.5°, 3.3°, and 6.3°. At higher angles, the $\Delta L=0$ component falls off and the $\Delta L=1$ components become larger, so the peak is small and broad. Also at higher angles the counting statistics are low so cross sections have larger statistical error. The peak areas are normalized to center of mass cross sections for

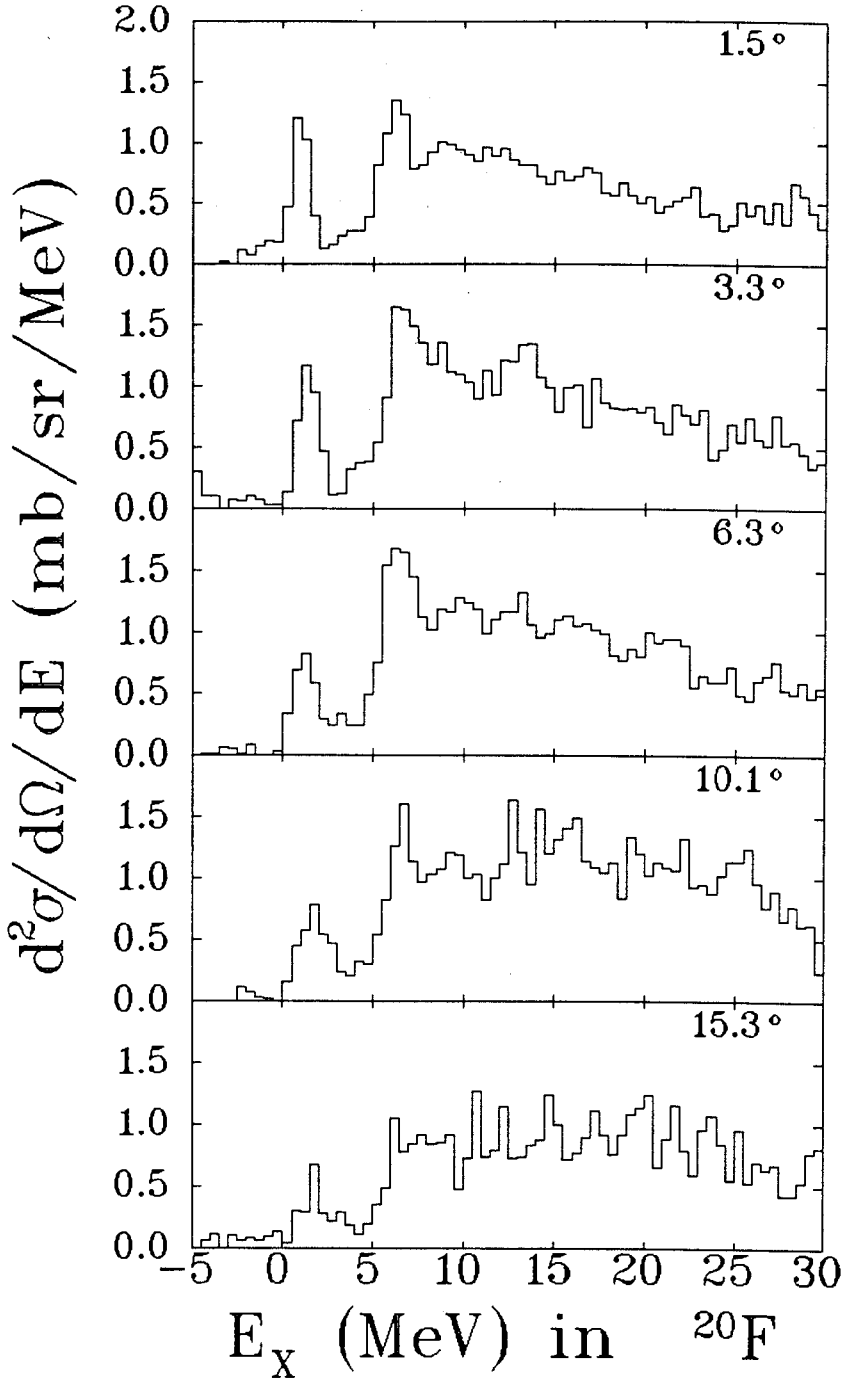

Figure 6.1: The $^{20}Ne(n,p)^{20}F$ spectra at E_n = 198 MeV at θ_{lab} =1.5°, 3.3°, 6.3°, 10.1°, and 15.3°. Center of mass cross sections are shown.

convenient comparison with theory. The cross sections are tabulated in table 6.1.

Table 6.1: Angular distribution of the 1.0 MeV peak in ^{20}F

θ_{lab}	θ_{cm}	q (fm^{-1})	$\sigma_{cm} : \sigma_{lab}$	σ_{lab} (mb/sr)	σ_{cm} (mb/sr)
1.53	1.63	0.0874	0.8890	1.69±0.25	1.50±0.22
3.34	3.54	0.1894	0.8891	1.70±0.25	1.51±0.22
6.30	6.68	0.3567	0.8895	1.41±0.23	1.25±0.20
10.1	10.72	0.5726	0.8906	1.37±0.26	1.23±0.23
15.3	16.22	0.8629	0.8927	0.73±0.15	0.65±0.13

A simple decomposition is then done by fitting the experimental angular distribution to theoretical angular distributions for the states that are predicted to make up the peak. The theoretical cross sections for individual states in the region of the 1.0 MeV peak have been calculated using the DWIA code DW81 [DW81]. The interaction used was the non-relativistic Love-Franey parameterization of the SP84 phase shift data of Arndt [FL 85]. The optical potential parameters are found from fits to proton elastic scattering data on ^{24}Mg and ^{28}Si at 200 and 280 MeV, scaled to E=200 MeV, A=20 [Lin 87,Hic+ 88]. The transition densities are from shell model wavefunctions calculated by OXBASH. The wavefunctions of the ground state and the 1^+, T=1 states were calculated using the universal *sd* shell interaction [Wil 84]. The states involved in ΔL=1 excitations (0^-, 1^-, and 2^-) were calculated by B.A.Brown using a Skyrme II interaction in a *s-p-sd-fp* basis, truncated to mixing of $1\hbar\omega$ excitations [Bro 87].

The largest contribution to the peak at low angles is the 1.0568 MeV 1^+, T=1 state, the analog of the well known 11.26 MeV state in ^{20}Ne [Ajz 87]. There are also three known states in this energy region which involve ΔL=1 transitions and cannot be resolved; a 1^- state at 0.9378 MeV and two 2^- states, one at 1.309 MeV and one at 1.843 MeV [Ajz 87]. These are the analogs of the 11.270 MeV 1^- T=1

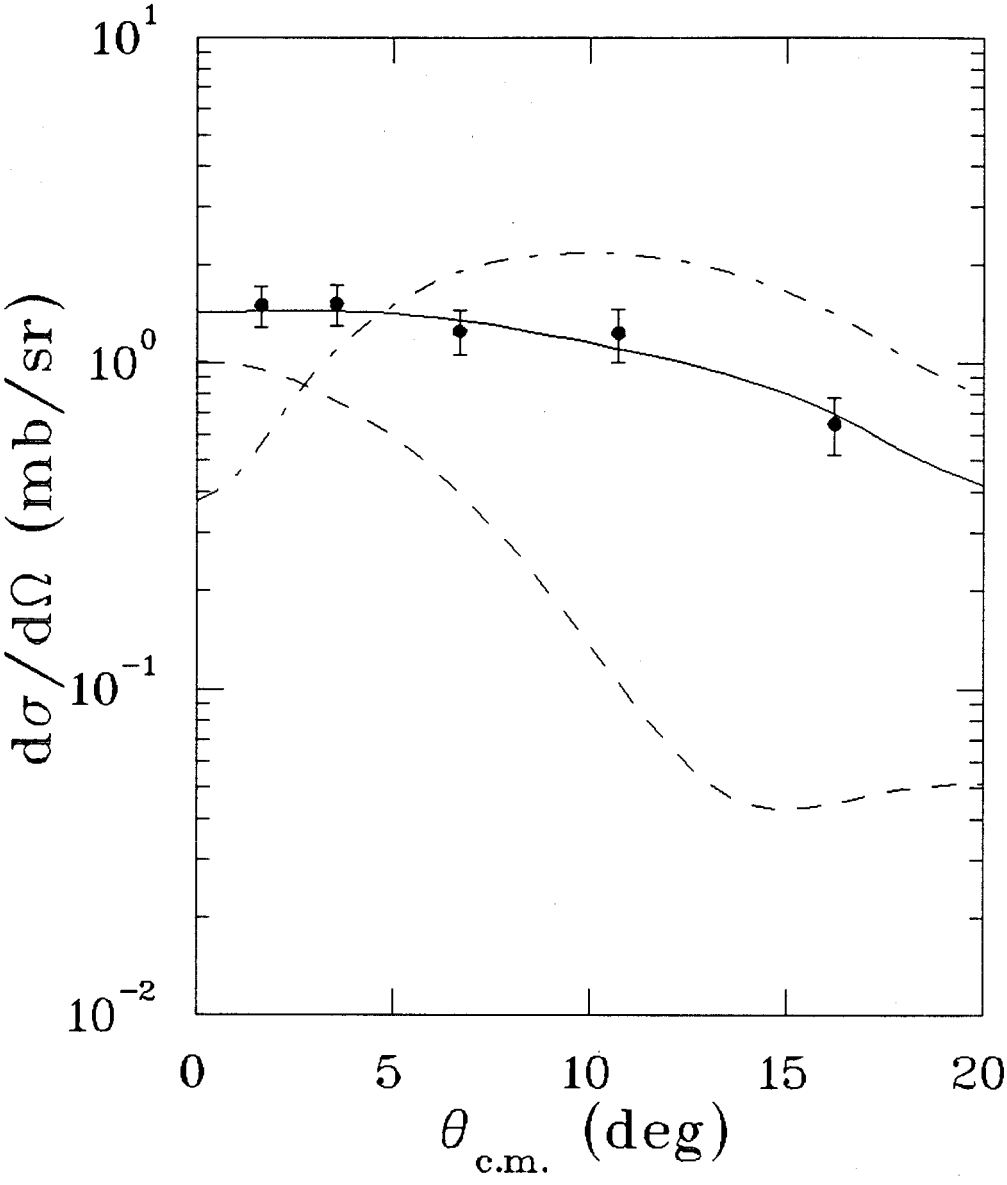

Figure 6.2: The angular distribution of the 1.0 MeV peak in ^{20}F . The points are the experimental cross sections, the solid line is the fit, the dashed line is the ΔL=0 shape and the dash-dot line is the ΔL=1 shape.

and the 11.60 MeV and 12.098 MeV 2^- T=1 states in ^{20}Ne , respectively. The 2^- states are clearly seen in (p,p') and (e,e') reactions [Wil+ 87,Ran+ 85]. Shell model calculations wrongly place these states at 15.53 and 15.83 MeV, probably because of the large basis used.

The experimental angular distribution is fit to the sum of two theoretical shapes: the theoretical angular distribution of the ΔL=0 transition to the 1.0 MeV 1^+ state and a ΔL=1 shape, which is just the sum of the theoretical shapes of three ΔL=1 states. Each of the shapes is convoluted with the finite angular acceptance. Figure 6.2 shows the fit to experimental data, σ(total)=A$\cdot\sigma(\Delta L=0)$+B$\cdot\sigma(\Delta L=1)$, as well as the ΔL=0 and ΔL=1 shapes used. The coefficients found from the fit are A=1.25$\pm$0.05 and B=0.45$\pm$0.05. The DWIA underpredicts the ΔL=0 cross section by 20% and overpredicts the ΔL=1 cross sections by about a factor of two. Once the ΔL=0 component is extracted the theoretical angular distributions from DWIA are used to extrapolate the ΔL=0 cross section to $\theta_{cm} = 0°$. The resulting cross section is

$$\sigma_{\Delta L=0}(\theta_{cm} = 0) = 1.25 \pm 0.18 \text{ mb/sr}.$$

6.1.2 Total Strengths

In order to extract the ΔL=0 cross sections, which are needed to find the GT strength, in a continuum of unresolved states it is necessary to do a full multipole decomposition of the spectra [Moi 87,Vet+ 89]. Such a procedure fits the angular distribution of each energy bin to theoretical angular distributions for transitions of different angular momentum transfer (multipolarity). For such a decomposition it is necessary to have experimental spectra at many angles, the number depending on how many multipolarities are to extracted. Theoretical shapes for each multipole to be extracted are also required. These shapes can also depend on the excitation energy.

For the present analysis the ΔL=0, ΔL=1 and ΔL$\geq$2 contributions were ex-

tracted. The ^{20}Ne(n, p)^{20}F spectra were measured at five angles out to θ_{lab}=15.3°, where the ΔL=2 strength is predicted to peak. The spectra are transformed to center of mass cross sections and are in 1.0 MeV bins. Three different sets of theoretical angular distribution shapes are used as input. The first set consists of the shapes of the single strongest transitions of each multipole in the region. The second set is from the incoherent sums of the angular distributions of all the predicted transitions of each multipole. The third set of shapes is from the coherent sums of the theoretical shapes, where each shape was normalized to unity before summing and averaging. The ΔL=0 angular distributions were calculated as above for the transitions from the 0^+, T=0 ground state (g.s.) of ^{20}Ne to the ten lowest 1^+, T=1 states. The ΔL=1 contributions come from strongest transitions from the g.s. to the 0^-, 1^-, and 2^-, T=1 states. These included one 0^-, three 1^-, and three 2^- states. The ΔL=2 shapes are $0\hbar\omega$ transitions to 2^+ and 3^+ states, which were calculated using the universal *sd* interaction. Only the ten lowest transitions to each 2^+ and 3^+ states were calculated.

The decomposition uses a least squares fitting routine, MINUIT, to fit the experimental angular distribution of each energy bin by the shapes of the multipole components. Examples of these fits are shown in figure 6.3. The decomposition yields the amount of each multipole component contributing to the cross section at each angle. The accuracy of the decomposition depends on the validity of the multipole shapes, and the statistics of the experimental spectra. The results of the decomposition using the coherently summed shapes are shown in figures 6.4 and 6.5.

A multipole decomposition was done using each of these sets of shapes for E_x=0–20 MeV and the results were almost identical in each case. For the final results the decomposition using the shapes from the coherent sums is used because it minimizes the continuum of ΔL=0 strength. The decomposition reveals that the ΔL=0 strength resides largely in the two peaks, which also have large contri-

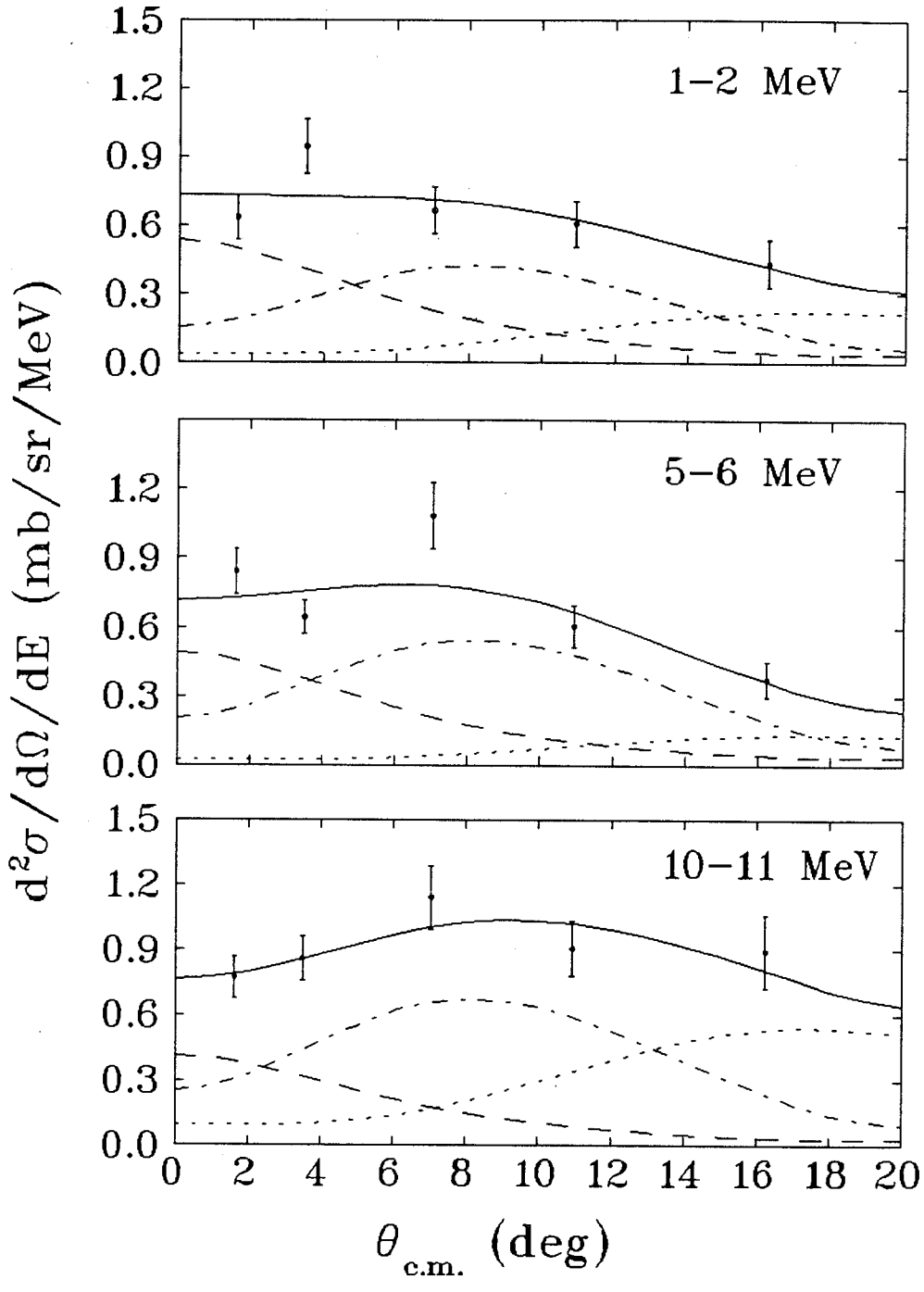

Figure 6.3: The fits to experimental angular distributions by the multipole decomposition for the 1–2 MeV (top) 5–6 MeV (middle) and 10–11 MeV (bottom) energy bins. The points are the experimental cross sections, the solid line is the fit. The dashed, dash-dot and the dotted lines are the ΔL=0, ΔL=1 and ΔL=2 components, respectively.

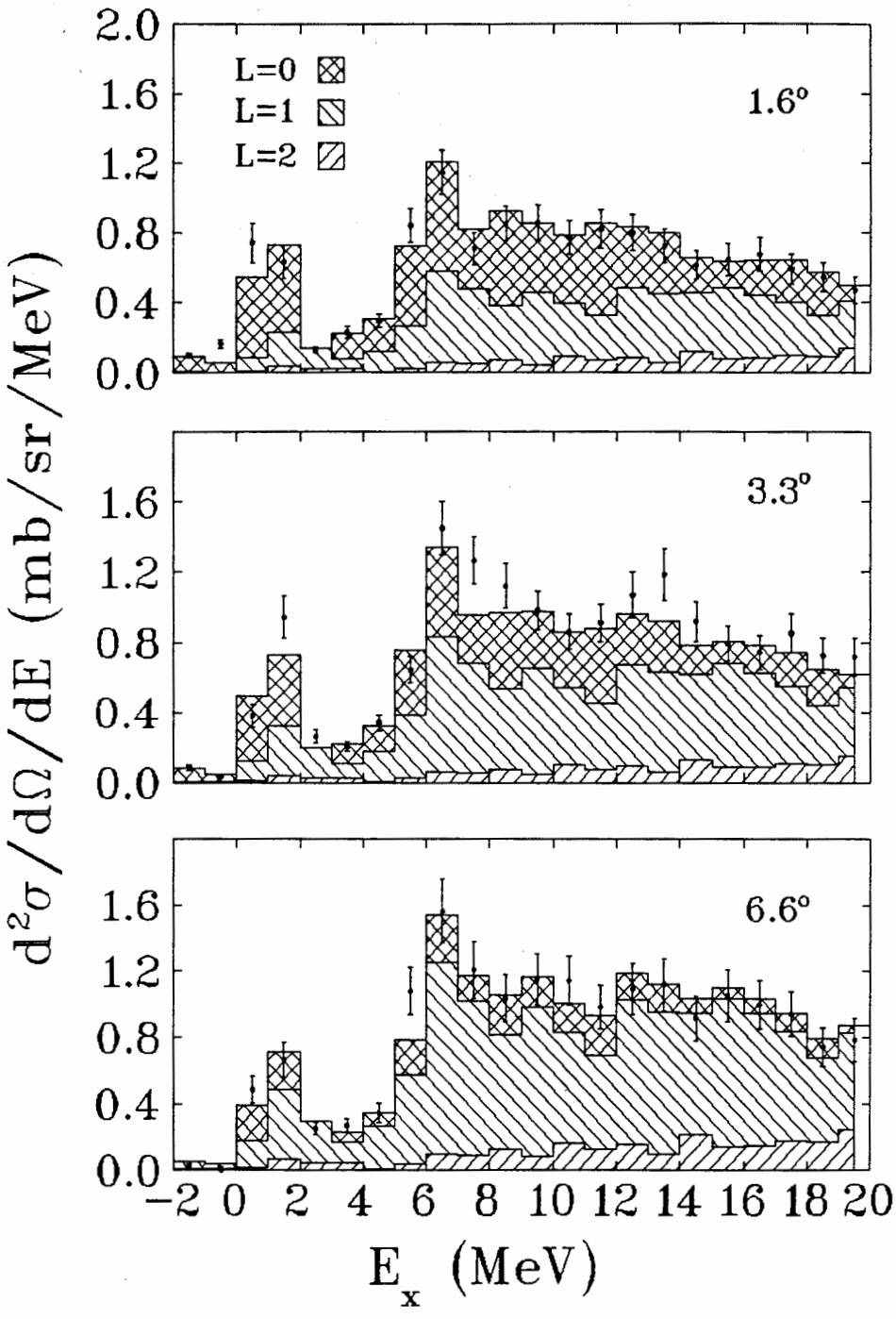

Figure 6.4: The multipole decomposition at θ_{lab} = 1.5°, 3.3°, and 6.3° for E_x=0–20 MeV. The different hatchings signify the different L-transfer contributions to the total spectrum.

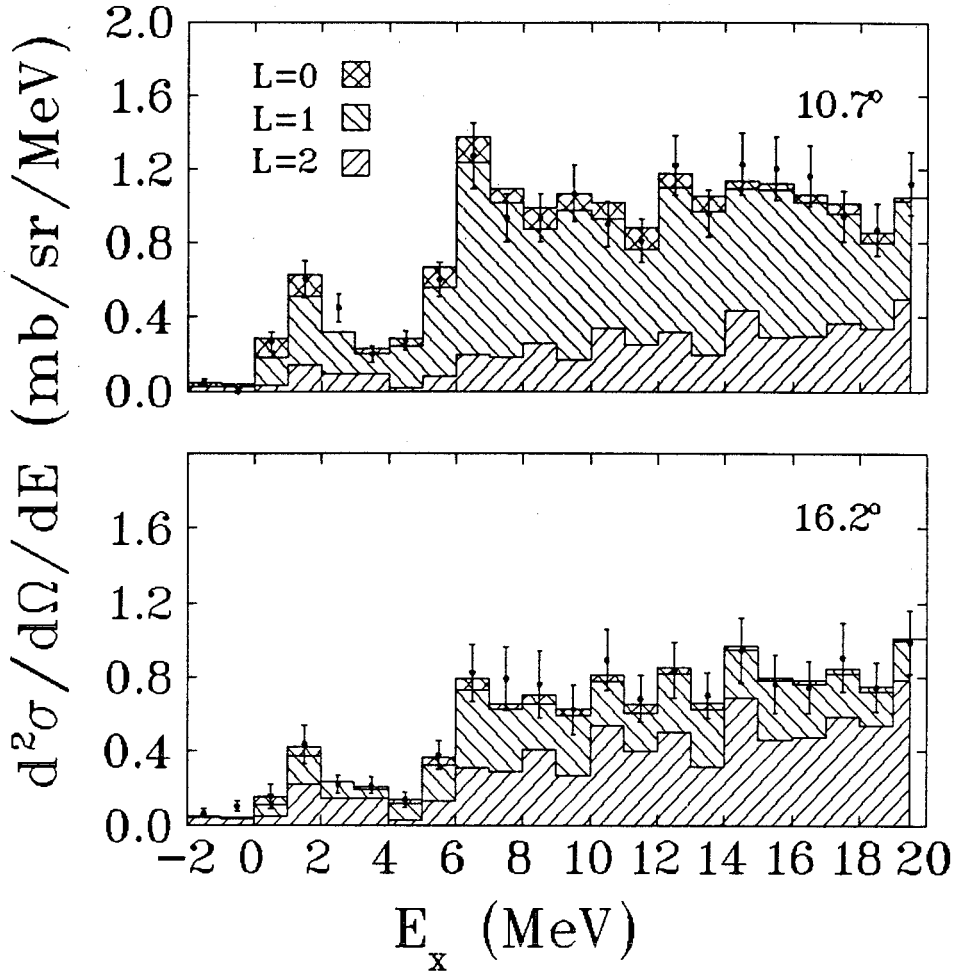

Figure 6.5: The multipole decomposition at θ_{lab} = 10.1°, 15.3° for E_x=0–20 MeV. The different hatchings signify the different L-transfer contributions to the total spectrum.

butions from the spin-dipole resonance (ΔT=1, ΔL=1, ΔS=1). Above 7.0 MeV the decomposition suggests a continuum of high lying ΔL=0 strength. Because the angular distributions in this region are fairly flat, and this continuum is not expected, the accuracy of the decomposition results are in doubt. The shell model calculations predict very little strength above 7.5 MeV.

This continuum of ΔL=0 strength is also seen in the multipole decomposition analysis of other (n,p) experiments. In the ^{15}N(n,p)^{15}C reaction at 290 MeV, where the GT strength is forbidden to first order, the multipole decomposition gives a continuum of ΔL=0 strength above 10.0 MeV [Cel 89]. A continuum of high lying ΔL=0 strength, which is not expected, is also extracted from the spectra of ^{54}Fe(n,p)^{54}Mn at 298 MeV [Vet+ 89]. In a recent analysis of ^{48}Ti(n,p)^{48}Sc at 200 MeV, the decomposition again yields a large amount of ΔL=0 strength at high excitation [Alf+ 89]. These results may suggest a problem with the extraction of ΔL=0 strength using multipole decompositions.

One cause of this ΔL=0 continuum could be the way the (n,p) spectra are normalized. The normalization uses the H(n,p) cross sections from the Arndt phase shifts, SAID (sec. 5.3.7). At large angles these cross sections may be too small, yielding lower values for experimental cross sections. Lower experimental cross sections at higher angles would decrease the amount of ΔL=1 and ΔL=2 contributions which would imply more ΔL=0 strength at low angles. Another, more likely, explanation is that there is a problem with the DWIA calculations of the theoretical angular distribution shapes. A recent experiment investigating single particle spin-dipole transitions in the ^{15}N(n,p)^{15}C reaction suggests that the theoretical shapes of ΔL=1 transitions from DWIA are wrong, the cross sections being too small at low angles [Cel 89]. The third possibility is that the small continuum of ΔL=0 strength is real, but is unaccounted for in the present shell model calculations. This could possibly be accounted for in higher order configuration mixing. No definitive conclusions seem possible at this time.

6.2 GT Strength from Cross Sections

The relationship between (n,p) cross sections and Gamow-Teller strength is discussed in section 2.2. The conclusion is that there is an approximate proportionality between the cross section at q=0 and $B(GT)$. The proportionality, (called $\hat{\sigma}^{+}_{GT}$ for (n,p) reactions and $\hat{\sigma}^{-}_{GT}$ for (p,n) reactions) is a function of the nucleus 'A', and incident particle energy E_p. This proportionality can be calculated by DWIA, but the values predicted have been shown to be unreliable [Tad+ 87]. Therefore, for nuclear structure studies, an empirical value of $\hat{\sigma}^{\pm}_{GT}$ is to be preferred.

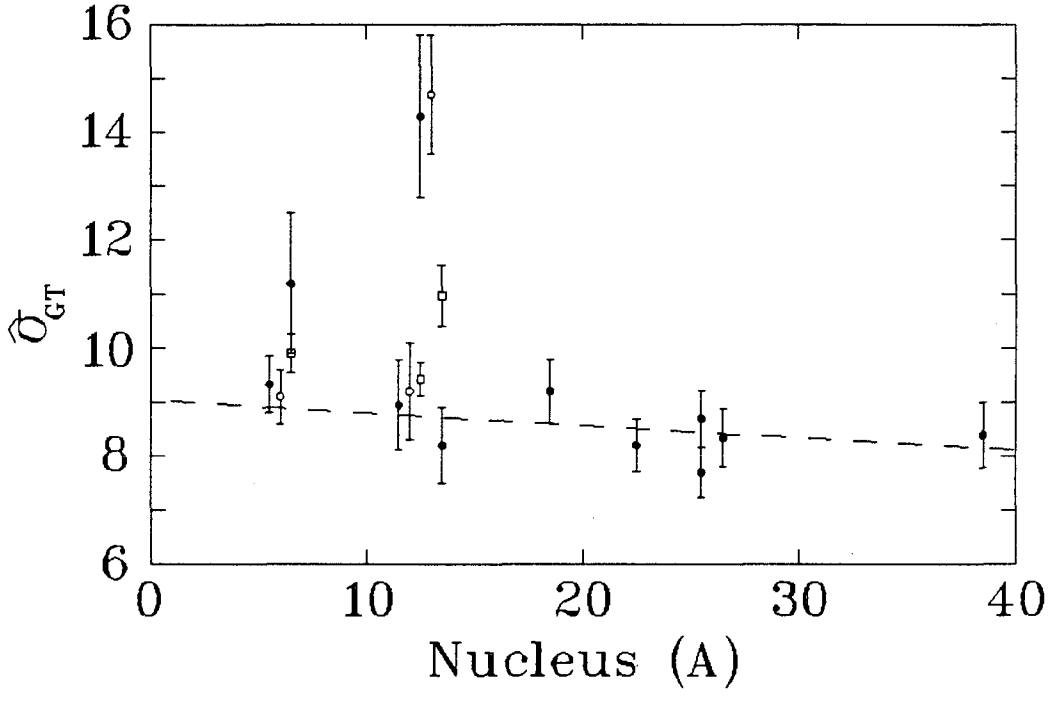

Figure 6.6: $\hat{\sigma}_{GT}$ determined from (p,n) reactions at E_p=160 MeV (filled circles) and (p,n) (open circles) and (n,p) reactions (open boxes) at 200 MeV. The dashed line is the fit to 160 MeV (p,n) data. Data from [Tad+ 87] and [Jac+ 88].

Experimentally, $\hat{\sigma}^{-}_{GT}$ and $\hat{\sigma}^{+}_{GT}$ are found by measuring the (p,n) and (n,p) cross sections of the peaks corresponding to a β decay for which the value ft was measured. The (p,n) data at 160 and 200 MeV and the (n,p) data at 200 MeV are shown in figure 6.6 [Tad+ 87,Jac+ 88]. In the p shell $\hat{\sigma}^{-}_{GT}$ from (p,n) agrees with

$\hat{\sigma}_{GT}^{+}$ from (n,p) for analogous transitions except for A=13. In the *sd* shell transitions in five nuclei have been measured by (p,n) at 160 MeV and $\hat{\sigma}_{GT}^{-}$ determined. This data is interpolated to A=20 to find $\hat{\sigma}_{GT}$ for ^{20}Ne . This value is scaled by an empirical value of $\hat{\sigma}_{GT}$(E=200 MeV)/$\hat{\sigma}_{GT}$(E=160 MeV) to get the value for A=20, E=200 MeV. The final value obtained is $\hat{\sigma}_{GT}$=9.0±.9 (mb/sr/B(GT)) which is used to extract the GT strength.

GT strengths can now be found from the experimental ΔL=0 cross sections. First the cross sections must be scaled to θ_{cm}, ω=0 using the theoretical shapes from DWIA. Once this is done the $B(GT)$ is found simply from

$$B(GT) = \sigma_{np}(\theta_{cm}, \omega = 0)/\hat{\sigma}_{GT}^{+} \tag{6.1}$$

The cross section of the ΔL=0 component of the 1.0 MeV peak from the fit to theoretical angular distributions was found to be

$$\sigma_{\Delta L=0}(\theta_{\rm cm} = 0) = 1.25 \pm 0.18 \text{ mb/sr}$$

Correcting to ω=0 the cross section becomes

$$\sigma_{\Delta L=0}(\theta_{\rm cm}, \omega = 0) = 1.35 \pm 0.20 \text{ mb/sr}$$

From this the $B(GT)$ is extracted

$$B(GT) = 0.150 \pm 0.027$$

This is also done for each energy bin of ΔL=0 spectrum extracted from the multipole decomposition. The results are listed in table 6.2.

The strength of the 1.0 MeV peak found from the multipole decomposition is

$$B(GT) = 0.131 \pm 0.029$$

which is less than that extracted from the fit peak decomposition. One reason for the difference is that in the multipole decomposition finite sized bins are used,

Table 6.2: Measured Cross sections and GT Strengths for E_x=0.0–10.0 MeV in ^{20}F.

E_x (MeV)	$\sigma_{cm}(1.5°)$ (mb/sr)	$\sigma_{\Delta L=0}(1.5°)$ (mb/sr)	$\sigma_{q=\omega=0}$ (mb/sr)	$B(GT^+)$
-0.50	0.165±0.024	0.056±0.013	0.063±0.015	0.007±0.002
0.50	0.745±0.113	0.491±0.104	0.559±0.118	0.062±0.013
1.50	0.636±0.098	0.539±0.126	0.623±0.145	0.069±0.016
2.50	0.129±0.019	0.000±0.057	0.000±0.066	0.000±0.007
3.50	0.230±0.031	0.148±0.042	0.178±0.050	0.020±0.006
4.50	0.295±0.038	0.196±0.053	0.240±0.065	0.027±0.007
5.50	0.841±0.099	0.494±0.120	0.617±0.150	0.069±0.017
6.50	1.146±0.127	0.666±0.178	0.853±0.228	0.095±0.025
7.50	0.710±0.092	0.367±0.133	0.480±0.174	0.053±0.019
8.50	0.852±0.103	0.575±0.141	0.772±0.189	0.086±0.021
9.50	0.857±0.102	0.430±0.144	0.593±0.197	0.066±0.022
10.50	0.775±0.097	0.419±0.133	0.592±0.188	0.066±0.021
Total				0.618±0.177

whereas the fit peak includes the tails and therefore sums the whole peak, giving larger cross sections. Also the multipole decomposition has a finite ΔL=2 component which lowers the strength in this peak, while the fit to theory did not include any. The large errors in both are a result of the small strengths being measured. The large uncertainty in $\hat{\sigma}_{GT}$ also contributes to the error. Since the cross sections and derived strengths from the fitted peak are expected to be more reliable they are used in the rest of the analysis.

6.3 Comparison to Theory

The measured $B(GT)$ can now be compared with theoretical predictions. From the calculated wavefunctions the transition densities and then $B(GT)$ and $B(M1)$ were calculated using both free-nucleon and effective one-body operators. The the-

oretical strengths are tabulated in appendix 2. Figure 6.7 shows theoretical values of $B(GT)$ compared with strength extracted by the multipole decomposition. For the state at 1.0 MeV the measured GT strength is 0.150±0.027 while calculations using free-nucleon operators predict a strength $B(GT)_{free}$=0.1424 and from effective operators $B(GT)_{eff}$=0.09847. If the quenching factor 'QF' is defined as

$$QF = \frac{B(GT)_{expt}}{B(GT)_{free}} \tag{6.2}$$

the quenching for this state is QF = 1.05±0.19. The shell model with free-nucleon operator predicts the strength of this state quite well.

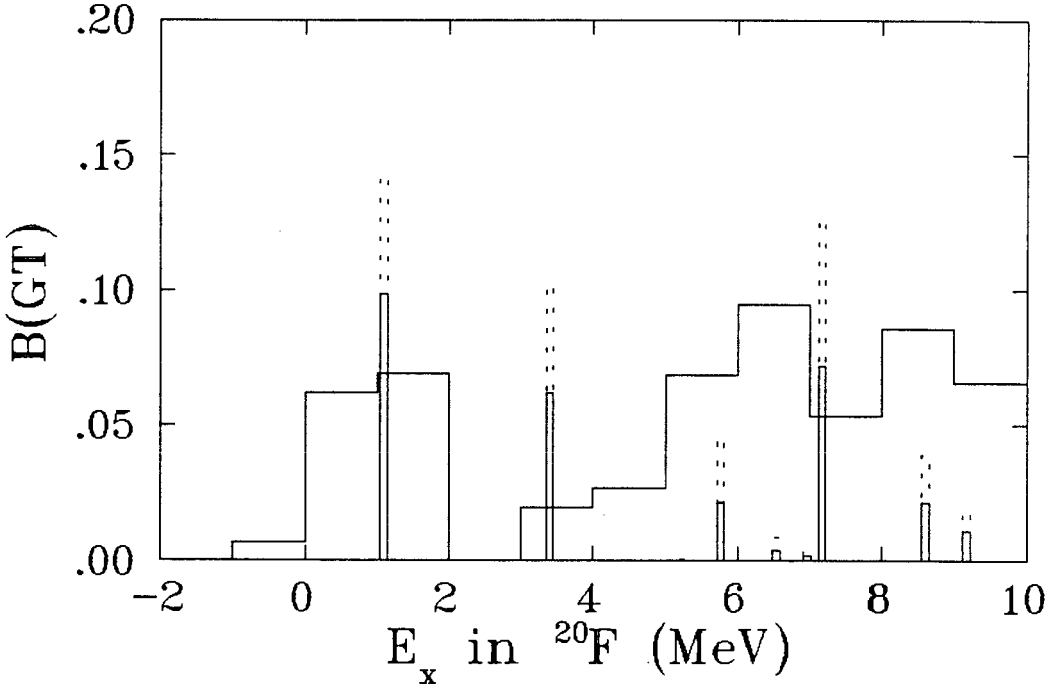

Figure 6.7: The derived GT strength (broad bins) compared with the calculated GT strength found using free-nucleon operators (narrow bins, dotted lines) and effective operators (narrow bins, solid lines).

For the other states there is a large uncertainty. No sharp peak is seen at 3.4 MeV where a strong state is predicted. The strength of this state is calculated to be $B(GT)$=0.1017 but the measured strength at this excitation energy is only

$B(GT)$=0.020±0.006. It is possible that the strong theoretical states at 5.7, 7.1 and 8.5 MeV are seen, but this can only be determined by comparing the total measured strength with the total predicted strength. Figure 6.7 shows the measured strength distribution compared with the shell model predictions. Clearly the shell model calculations do not reproduce the strength distribution very well. In figure 6.8 the running sum of the measured $B(GT)$ for E_x=0–10 MeV in ^{20}F is compared those from theory. The theoretical values exhibit steps where the peaks are predicted but the experimental increments occur at 1.0 MeV intervals because of the finite bin size. The comparison shows that, if the decomposition is believed, the experiment agrees with the predictions using free-nucleon operators, and no net quenching is seen. Over the whole region included in the shell model calculations, E_x=0–10 MeV, the QF would be 1.27±0.36. A more conservative estimate would include only the region where there is significant GT strength predicted. This would minimize the contribution from the ΔL=0 continuum. Since there is a strong excitation predicted at 7.13 MeV, the region of comparison can be truncated to E_x=0–7.5 MeV. In this region QF = 0.93±0.26. This conservative result will be used to define the total quenching.

6.4 Comparison with M1 Strength

The direct comparison of GT and M1 strength can show the effects of spin-orbital interference and/or meson exchange currents on the M1 matrix element (sec. 2.1). To compare $B(M1)$ and $B(GT)$ it is necessary to convert $B(GT)$ values to $B(M1)$ values. A simple relationship between the M1 and GT operators can be found for pure spin-flip transitions, such as those seen in (n,p) reactions at low q [And+ 87]. From this relationship a pure spin M1 strength, '$B(\sigma)$' is defined. It is found that for N=Z nuclei,

$$B(\sigma) = B(GT) \cdot 2.6435\ \mu_n^2 \tag{6.3}$$

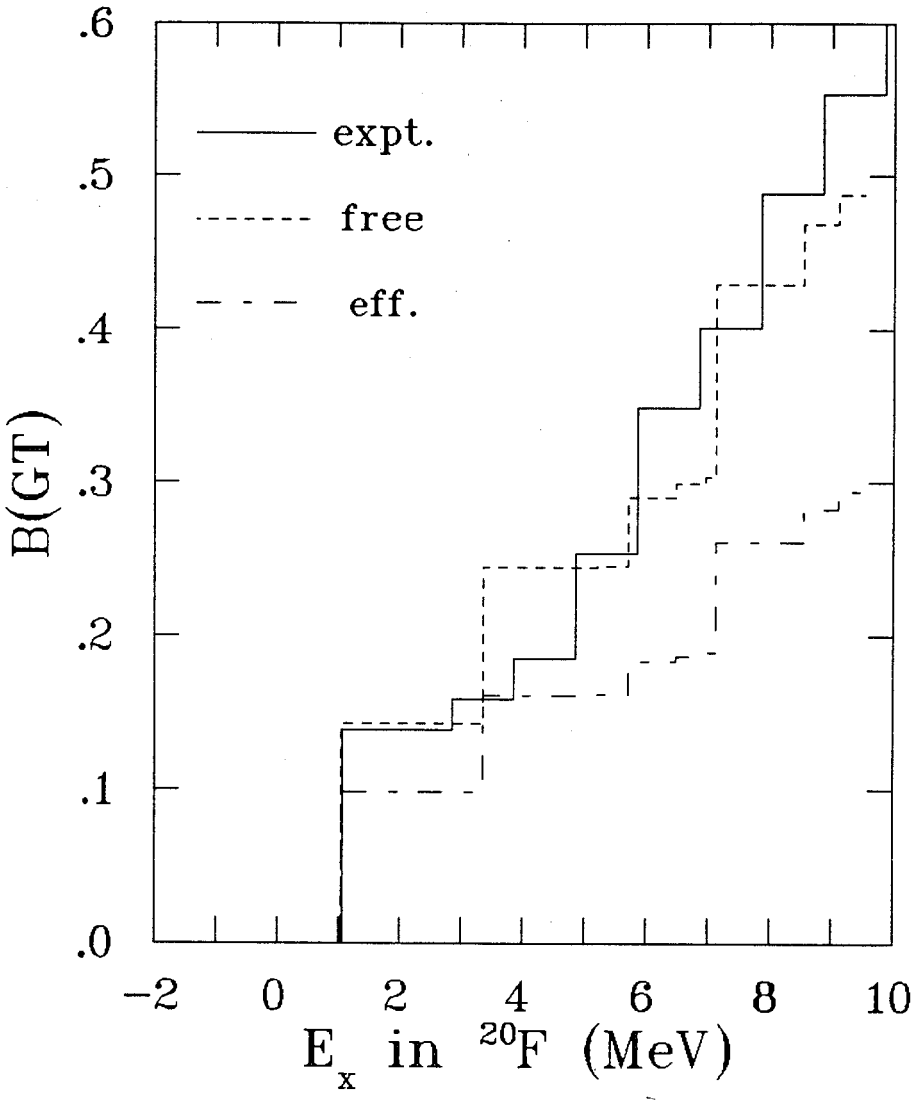

Figure 6.8: The running sums of $B(GT)$ vs. E_x in ^{20}F from experiment (solid lines) and shell model calculations using free (dashed line) and effective (dash-dot line) operators.

The M1 and GT strengths are best compared by finding the ratio of $B(M1)$ to $B(\sigma)$, i.e.

$$R_\sigma = B(M1)/B(\sigma) \tag{6.4}$$

This ratio gives a dimensionless measure of the enhancement from the orbital and MEC contributions, such that if there was no orbital or MEC contribution R_σ would be unity. Unfortunately the individual contributions cannot be extracted separately.

The M1 strength in ^{20}Ne has been measured by two reactions, (e, e') and (γ, γ'). The (γ, γ') reaction is limited by the particle emission threshold to states with $E_x \leq 13.0$ MeV in ^{20}Ne. Experiments using both probes only see the 11.26 MeV 1^+, T=1 state [Ben+ 71,Ber+ 83,Ber+ 84]. For this state it is found that $B(M1) = 2.02 \pm 0.36\ \mu_n^2$. The shell model predicts $B(M1) = 1.96\ \mu_n^2$ using free-nucleon operators and $B(M1) = 2.32\ \mu_n^2$ using the effective operator. The experimental results are in good agreement with the free-nucleon operator predictions which is consistent with the results for $B(GT)$. Using both experimental results, $R_\sigma = 5.1 \pm 1.3$. This shows the large effect of the orbital component in the M1 matrix element. When compared with 5.21 and 8.92, from calculations with free and effective one-body operators, respectively, again the predictions using the free-nucleon operator are better.

6.5 Comparison to Results from Other Probes

Three other hadronic probes have been used to measure $B(GT)$ in ^{20}Ne . The earliest measurement was made using the $^{20}\mathrm{Ne}(\pi^-, \gamma)^{20}\mathrm{F}$ reaction [Mar+ 81]. This probe could only measure up to $E_x = 7.0$ MeV in ^{20}F because of the particle emission threshold. Because this reaction involves higher momentum transfers the states with higher L-transfer are more strongly populated. The only 1^+ state is seen at 1.0 MeV. The branching ratio to this state is related to the spin matrix element. From this it is found that $B(\sigma) = 0.425 \pm 0.128$ or $B(GT) = 0.1607 \pm 0.030$, which

is consistent with the (n,p) results. A state is also seen at 6.0 MeV in ^{20}F and, whereas the authors assigned this to be 2^-, Rangacharyulu *et al.*later suggested that this state might have a large component of ΔL=0 strength [Ran+ 85].

The most thorough study of spin-isospin excitations in ^{20}Ne has been done by the ORSAY group using high resolution inelastic (p,p') at low momentum transfer [Wil+ 87]. This group sees three distinct 1^+ peaks, at 11.26 MeV, 13.5 MeV and 15.7 MeV. This is inconsistent with the (n,p) results which only sees no significant strength at 3.4 MeV in ^{20}F (=13.5 MeV in ^{20}Ne). The cross sections were measured from $\theta_{\rm lab}$ = 3.0° to 10°. For the 11.26 MeV state they give $B(\sigma)$=0.49 $\pm$0.06μ_n^2 or $B(GT)$=0.185$\pm$0.023. Although their strength is larger than the (n,p) results, the cross sections are in agreement with the (n,p) data, when the factor of two from the isospin Clebsch-Gordan coefficient is taken into account. For the other states the agreement with theoretical cross sections is good, although the 1^+ assignment of the state at 15.7 MeV is somewhat uncertain. They see no evidence of any 1^+ strength above 17.0 MeV but are uncertain because the continuum background due to the kapton windows on their target obscures the spectra at excitation above 17 MeV. If the state predicted to be at 17.3 MeV is ignored they have a QF of 1.0$\pm$0.1 but if it is included the QF is 0.7.

There have been two measurements of the ^{20}Ne(p,n)^{20}Na reaction at intermediate energies, both at done IUCF. The first was done by the LAMPF group at E_p=160 MeV [Dev+ 82,Rap 89]. A strong peak was reported at 0.9 MeV in ^{20}Na which is the analog of the transition to the 1^+, T=1 11.26 MeV state in ^{20}Ne . A preliminary analysis assigns a $B(GT) \sim 0.12$ for this state. A second weaker and broader peak was seen at 6.0 MeV. The angular distribution suggested that it had components of both ΔL=0 and ΔL=1. The final results of this experiment have not been published. The second experiment was done by the Kent State group at 136 MeV with a resolution of 336 keV [And 89,Tam+ 89]. Preliminary analysis yields $B(GT)$ =0.403 for E_x=0–12.0 MeV which implies a quenching factor of 0.7.

The final results are also not yet available.

6.6 Comparison with Other *sd* Shell Nuclei

The systematics of quenching in the *sd* shell have been experimentally explored by various groups using different probes. The major work was done by TRIUMF using (p,p′) and (n,p) , ORSAY using (p,p′) , and IUCF (two groups) using (p,n). The TRIUMF (p,p′) work consists of the measurements of the $(\vec{p},\vec{p}')$ reaction on ^{24}Mg and ^{28}Si [Saw+ 88,Hau+ 88]. The $(\vec{p},\vec{p}')$ reaction uses polarized protons and measures the spin-transfer parameters, along with the cross sections, to identify the transitions that involved spin-flips. The TRIUMF (n,p) experiments consist of (n,p) reactions on ^{24}Mg, ^{26}Mg and now ^{20}Ne [Hau 89,Hel 89]. The analysis of experiments on the Mg isotopes are still only preliminary.

The ORSAY group has studied spin-isospin excitations in many *sd* shell nuclei using (p,p′) reactions at E_p=201 MeV [Wil+ 87,Cra+ 89]. Their analysis, however, has been criticized on the grounds that the extraction of GT strength relies too much on theory. There is also some difficulties in distinguishing between 1^+, T=0 from T=1 states on the basis of angular distributions. The IUCF (p,n) work is the most extensive and consistent yet. Both the LAMPF group and the Kent state group have studied GT strength in many *sd* shell nuclei [Tad+ 87,Rap 89] [And+ 82,And+ 87] [Mad+ 87,And 89].

The results of all the work is shown in figure 6.9. The quenching factors found by the ORSAY group show a large scatter, which could be a result of errors in their analysis. The IUCF and TRIUMF work (except the present analysis) shows most quenching on the order of 60–70%. These results are consistent with the quenching predicted by the effective operator, or a renormalization of the ratio of the weak coupling constants to $g_A/g_V \approx 1.0$.

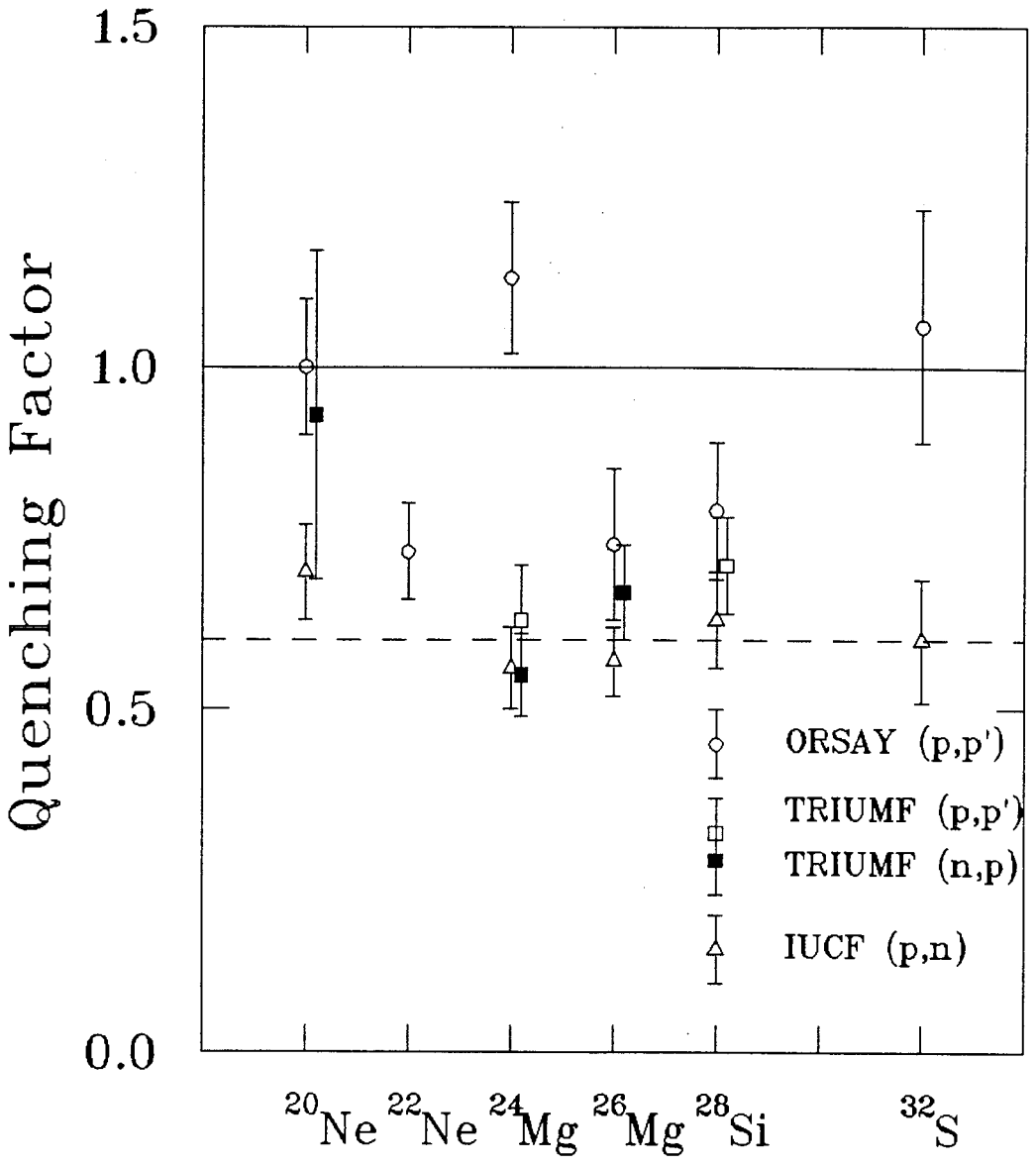

Figure 6.9: The quenching factors of different nuclei in the *sd* shell from IUCF, ORSAY, and TRIUMF. The dashed line represents a quenching of 60%. References are in the text.

6.7 Conclusions

The main purpose of the present work was to measure the GT strength in the A=20 system using the ^{20}Ne(n, p)^{20}F reaction at E_n = 198 MeV . This has been done and the GT strength is found for E_x=0–10 MeV in ^{20}F . The strength of the 1^+ state at 1.0 MeV was found to be well described by shell model wavefunctions and the one-body free-nucleon operator. The GT strength found from the full multipole decomposition indicates no quenching of strength in the region E_x=0–7.5 MeV. However the strength distribution was not well reproduced by the theory. Much of the strength seen experimentally is in a continuum that comes out of the multipole decomposition. The proper interpretation of this continuum is unclear.

Another purpose of the experiment was to see the dramatic effects of the spin-orbital interference in the M1 matrix element. The M1 strength of the 11.26 MeV state in ^{20}Ne seen in 180° electron scattering is enhanced by a factor of five over the M1 strength involving only the spin operator. This enhancement is also well predicted by free-nucleon operators. These results cannot be used to extract any information about MECs in nuclei by themselves since both the orbital and any MEC contribution could be responsible for the enhancement, and there is no way of determining their contributions separately. The systematics of quenching all across the *sd* shell must be studied to test the consistency of the shell model calculations before the effects of MEC can be examined. The quenching in ^{20}Ne seen in the present experiment is less than that seen in most other *sd* shell nuclei. Whereas the quenching is usually on the order of 60–70%, none is seen in ^{20}Ne .

These results are tempered by the large uncertainties present. The quenching factor is uncertain to 25%, so it is almost meaningless. There are many reasons for this large error. The main problem is that small strengths were measured. Much more data would be required to decrease the statistical uncertainties significantly. Another problem is that the resolution did not permit individual states to be resolved. This means that to extract the total GT strength the multipole

decomposition had to be done. The use of such decompositions is quite problematic, especially when starting with data of low statistics. It is important to resolve the issue of the high lying $\Delta L=0$ continuum, seen in many (n,p) experiments, to properly interpret the extracted strengths. In the case of ^{20}F , if the continuum of $\Delta L=0$ strength disappeared, most of the $\Delta L=0$ strength would in turn vanish. Most of remainder would be in the large peak at 1.0 MeV with a little in the peak at 6.5 MeV. If only the strength of 1.0 MeV state is taken to be real the quenching would be more than 60%. Future work on isovector excitations may bring the necessary insight.

One other major result of this experiment was the development of the (n,p) gas target. This target has shown itself reliable in many experiments and is now an integral part of the TRIUMF CHARGEX facility. It will be one tool used to continue the work and further extend our knowledge of the structure of nuclei.

Appendix 1.

The final ^{20}Ne(n, p)^{20}F center of mass cross sections at $\theta_{cm} = 1.62°$

E_x (MeV)	σ_{cm}	$\Delta\sigma_{cm}$
-1.5000	0.0989	0.0156
-0.5000	0.1649	0.0243
0.5000	0.7446	0.1132
1.5000	0.6364	0.0979
2.5000	0.1292	0.0189
3.5000	0.2297	0.0313
4.5000	0.2951	0.0377
5.5000	0.8412	0.0992
6.5000	1.1462	0.1274
7.5000	0.7100	0.0921
8.5000	0.8515	0.1028
9.5000	0.8571	0.1021
10.5000	0.7750	0.0966
11.5000	0.8212	0.1091
12.5000	0.8013	0.1016
13.5000	0.7226	0.0974
14.5000	0.6134	0.0820
15.5000	0.6441	0.0911
16.5000	0.6738	0.0963
17.5000	0.5922	0.0874
18.5000	0.5459	0.0818
19.5000	0.4714	0.0760
20.5000	0.4387	0.0725
21.5000	0.4471	0.0771
22.5000	0.5300	0.0940
23.5000	0.3624	0.0660
24.5000	0.2716	0.0569
25.5000	0.4090	0.0806
26.5000	0.3732	0.0718
27.5000	0.3762	0.0741
28.5000	0.5426	0.1007
29.5000	0.3275	0.0737

The final ^{20}Ne(n, p)^{20}F center of mass cross sections at $\theta_{cm} = 3.3°$

E_x (MeV)	σ_{cm}	$\Delta\sigma_{cm}$
-1.5000	0.0858	0.0150
-0.5000	0.0333	0.0103
0.5000	0.3828	0.0651
1.5000	0.9445	0.1190
2.5000	0.2632	0.0390
3.5000	0.2045	0.0295
4.5000	0.3422	0.0454
5.5000	0.6440	0.0746
6.5000	1.4506	0.1518
7.5000	1.2672	0.1335
8.5000	1.1229	0.1267
9.5000	0.9830	0.1107
10.5000	0.8598	0.1003
11.5000	0.9114	0.1048
12.5000	1.0706	0.1317
13.5000	1.1868	0.1486
14.5000	0.9180	0.1110
15.5000	0.7928	0.0978
16.5000	0.7437	0.0969
17.5000	0.8517	0.1111
18.5000	0.7249	0.1025
19.5000	0.7180	0.1055
20.5000	0.6856	0.0957
21.5000	0.6552	0.0942
22.5000	0.6503	0.1025
23.5000	0.5393	0.0889
24.5000	0.5230	0.0940
25.5000	0.5749	0.0953
26.5000	0.4843	0.0914
27.5000	0.5784	0.1048
28.5000	0.4508	0.0900

The final ^{20}Ne(n, p)^{20}F center of mass cross sections at $\theta_{cm} = 6.6°$

E_x (MeV)	σ_{cm}	$\Delta\sigma_{cm}$
-1.5000	0.0252	0.0158
-0.5000	0.0026	0.0191
0.5000	0.4852	0.0802
1.5000	0.6664	0.1043
2.5000	0.2523	0.0382
3.5000	0.2699	0.0420
4.5000	0.3457	0.0574
5.5000	1.0805	0.1443
6.5000	1.5633	0.1927
7.5000	1.2072	0.1711
8.5000	1.0377	0.1415
9.5000	1.1541	0.1542
10.5000	1.1415	0.1461
11.5000	0.9864	0.1314
12.5000	1.0941	0.1527
13.5000	1.1207	0.1573
14.5000	0.9145	0.1334
15.5000	1.0533	0.1546
16.5000	0.9998	0.1471
17.5000	0.9428	0.1357
18.5000	0.7413	0.1176
19.5000	0.7838	0.1307
20.5000	0.8967	0.1524
21.5000	0.8907	0.1563
22.5000	0.6806	0.1235
23.5000	0.5804	0.1096
24.5000	0.6180	0.1206
25.5000	0.4379	0.1014
26.5000	0.5881	0.1268
27.5000	0.6052	0.1409
28.5000	0.5128	0.1313
29.5000	0.4777	0.1253

Appendix 1. (cont'd)

The final ^{20}Ne(n, p)^{20}F center of mass cross sections at $\theta_{cm} = 10.72°$

E_x (MeV)	σ_{cm}	$\Delta\sigma_{cm}$
-1.5000	0.0487	0.0183
-0.5000	0.0000	0.0197
0.5000	0.2695	0.0523
1.5000	0.6084	0.1003
2.5000	0.4531	0.0760
3.5000	0.2017	0.0439
4.5000	0.2767	0.0525
5.5000	0.6058	0.0897
6.5000	1.2760	0.1794
7.5000	0.9384	0.1296
8.5000	0.9381	0.1304
9.5000	1.0717	0.1545
10.5000	0.9073	0.1242
11.5000	0.8128	0.1161
12.5000	1.2258	0.1620
13.5000	0.9617	0.1267
14.5000	1.2300	0.1702
15.5000	1.2077	0.1723
16.5000	1.1644	0.1637
17.5000	0.9439	0.1378
18.5000	0.8728	0.1398
19.5000	1.1225	0.1710
20.5000	0.9523	0.1408
21.5000	0.9550	0.1474
22.5000	0.9963	0.1482
23.5000	0.8086	0.1291
24.5000	0.9551	0.1479
25.5000	1.0530	0.1631
26.5000	0.7645	0.1365
27.5000	0.6903	0.1281
28.5000	0.6123	0.1273
29.5000	0.3830	0.0991

Appendix 1. (cont'd)

The final ^{20}Ne(n, p)^{20}F center of mass cross sections at $\theta_{cm} = 16.2°$

E_x (MeV)	σ_{cm}	$\Delta\sigma_{cm}$
-1.5000	0.0647	0.0257
-0.5000	0.1017	0.0263
0.5000	0.1567	0.0639
1.5000	0.4348	0.1035
2.5000	0.2221	0.0469
3.5000	0.2153	0.0451
4.5000	0.1396	0.0413
5.5000	0.3771	0.0766
6.5000	0.8228	0.1573
7.5000	0.7905	0.1711
8.5000	0.7623	0.1820
9.5000	0.6237	0.1339
10.5000	0.8943	0.1671
11.5000	0.6846	0.1265
12.5000	0.8395	0.1490
13.5000	0.7026	0.1263
14.5000	0.9462	0.1755
15.5000	0.7636	0.1576
16.5000	0.7457	0.1404
17.5000	0.9071	0.1840
18.5000	0.7462	0.1363
19.5000	0.9903	0.1726
20.5000	0.8459	0.1548
21.5000	0.9074	0.1668
22.5000	0.6205	0.1282
23.5000	0.9060	0.1647
24.5000	0.6221	0.1340
25.5000	0.6648	0.1474
26.5000	0.5966	0.1319
27.5000	0.4883	0.1089
28.5000	0.4243	0.1184
29.5000	0.7035	0.2016

Appendix 2.

$B(GT)$ and $B(M1)$ of first ten 1^+, T=1 states in ^{20}Ne using free nucleon and effective operators and new wavefuctions from Brown [Bro 87].

E_x (MeV)	$B(GT)_{free}$	$B(GT)_{eff}$	$B(M1)_{free}$ (μ_N^2)	$B(M1)_{eff}$ (μ_N^2)
11.196	.14233	.09847	1.95862	2.32307
13.496	.10168	.06211	0.03698	0.00319
15.030	.00025	.00034	0.02483	0.03714
15.359	.00076	.00012	0.00548	0.00018
15.863	.04505	.02177	0.05293	0.00497
16.639	.00858	.00387	0.05100	0.01854
17.114	.00418	.00219	0.00158	0.00821
17.269	.12634	.07196	0.00372	0.01041
18.705	.03929	.02168	0.02290	0.00211
19.266	.01872	.01132	0.17981	0.15944
Total	.48728	.29383	2.33786	2.56486

References

[Ajz 87] F.Ajzenberg-Selove, *Nucl. Phys. A475* (1987) 117

[Alf+ 86a] W.P.Alford *et al.*, *AIP Conf. Proc. 150* (1986) 710

[Alf+ 86b] W.P.Alford *et al.*, *Phys. Lett. B179* (1986) 20

[Alf+ 89] W.P.Alford *et al.*, to be published

[And+ 82] B.D.Anderson *et al.Phys. Rev. C26* (1982) 8

[And+ 87] B.D.Anderson *et al.Phys. Rev. C36* (1987) 2195

[And 89] B.D.Anderson *private communication* 1989

[Ari+ 88] A.Arima, K.Shimzu, W.Bentz, and H.Hyuga, *Adv. in Nucl. Phys. 18* (1987) 1

[AS 84] R.A.Arndt and L.D.Soper, *Scattering Analysis Interactive Dial-in* (SAID) program, 1984, unpublished

[AW 61] J.D.Anderson and C.Wong, *Phys. Rev. Lett. 7* (1961) 250

[Bac+ 86] D.Bachelier *et al.*, *Phys. Lett. B172* (1986) 23

[Ben+ 71] W.L.Bendel, L.W.Fagg, S.K.Numrich, E.C.Jones,Jr., and H.F.Kaiser, *Phys. Rev. C3* (1971) 1821

[Ber+ 83] U.E.P.Berg, K.Ackermann, K.Bangert, R.Stock, and K.Wienhard, *Phys. Rev. C27* (1983) 2981

[Ber+ 84] U.E.P.Berg, K.Ackermann, K.Bangert, C.Bläsing, W.Naatz, M.K.Brussel, T.E.Chapuran, and B.H.Wildenthal, *Phys. Lett. B140* (1984) 191

[BE 87] G.F.Bertsch and H.Esbensen *Rep. Prog. Phys. 50* (1987) 607

[Bro 87] B.A.Brown *private communication* 1987-89.

[BW 83] B.A.Brown and B.H.Wildenthal, *Phys. Rev. C28* (1983) 2397

[BW 85] B.A.Brown and B.H.Wildenthal, *At. Data Nucl. Data Tables 33:* (1985) 347

[BW 87] B.A.Brown and B.H.Wildenthal, *Nucl. Phys. A474* (1987) 290

[BW 88] B.A.Brown and B.H.Wildenthal, *Ann. Rev. Nucl. Part. Sci. 1988.38* (1988) 29-66

[Cel 89] A.Celler *et al.*to be published, and *private communication* 1989

[Cra+ 89] G.M.Crawley, C.Djalali, N.Marty, M.Morlet, A.Willis, N.Anantaraman, B.A.Brown, and A.Galonsky, *Phys. Rev C39* (1989) 311

[Dev+ 82] R.P.DeVito, C.C.Foster, C.D.Goodman, T.N.Taddeucci, S.M.Austin, A.Galonsky, and U.E.P.Berg, *I.U.C.F. Ann. Rep. 1982* 32

[Doe+ 75] R.R.Doering *et al.*, *Phys. Rev. Lett. 35* (1975) 1691

[DW81] Computer code DW81, Arizona State University, J.R.Comfort

[Etc+ 85] A.Etchegoyen *et al.MSU-NSCL Rep.* (1985) 524

[FL 85] M.A.Franey and W.G.Love, *Phys. Rev. C31* (1985) 488

[Gaa +80] C.Gaarde, J.S.Larsen, M.N.Harakeh, S.Y.Van Der Werf, M.Igarashi, and A.Muller-Arnke, *Nuc. Phys. A334* (1980) 248

[Hau+ 88] O.Häusser *et al.Phys. Rev. C37* (1988) 1119

[Hau 89] O.Häusser *private communication* 1989

[Hic+ 88] K.H.Hicks *et al.*, *Phys. Rev. C38* (1988) 229

[Hel 87] R.Helmer *Can. J. Phys. 65* (1987) 588

[Hel 89] R.Helmer *private communication* 1989

[Hen+ 87] R.S.Henderson *et al.*, *Nucl. Inst. and Methods A257* (1987) 97

[Hen+ 89] R.S.Henderson *et al.*, submitted to *Nucl. Inst. and Methods*

[Ike+ 63] K.I.Ikeda, S.Fujii, and J.I.Fujita, *Phys. Lett. 3* (1963) 271

[Jac+ 88] K.P.Jackson *et al.*, *Phys. Lett. B201* (1988) 25

[LF 81] W.G.Love and M.A.Franey, *Phys. Rev. C24* (1981) 1073

[Lin 87] C.C.K.Lin unpublished M.Sc thesis 1987

[KM 83] W.Knüpfer and B.C.Metsch *Phys. Rev. C27* (1983) 2487

[Mad+ 87] R.Madey *et al.Phys. Rev. C35* (1987) 2011

[Mar+ 81] C.J.Martoff *et al.*, *Phys. Rev. Lett. 46* (1981) 891

[Moi 87] M.A.Moinester, *Can. J. Phys. 65* (1987) 660

[MRS] MRS Manual, TRIUMF, unpublished

[OR 79] E.Oset and M.Rho, *Phys. Rev. Lett. 42* (1979) 47

[Rap 89] J.Rapaport in *Fundamental Symmetries and Nuclear Structure* eds. J.N.Ginocchio and S.P.Rosen (World Scientific, Singapore, 1989)

[Ran+ 85] C.Rangacharyulu, E.J.Ansaldo, D.Stockhausen, D.Bender, S.Müller, A.Richter, N.Lo Iudice, and F.Palumbo, *Phys. Rev. C31* (1985) 1656

[Ric 89] A.Richter *Private Communication*

[Saw 87] R.Sawafta *unpublished Ph.D Thesis* (1987)

[Saw+ 88] R.Sawafta *et al.Phys. Lett. B201* (1988) 219

[Tad+ 87] T.N.Taddeucci, C.A.Goulding, T.A.Carey, R.C.Byrd, C.D.Goodman, C.Gaarde, J.Larsen, D.Horen, J.Rapaport, E.Sugarbaker, *Nucl. Phys. A469* (1987) 125

[Tam+ 89] N.T.Tamimi *et al.*, *Bull. of the Amer. Phys. Soc. 34* (1989) 1233

[TK 83] I.S.Towner and F.C.Khanna, *Nucl. Phys. A399* (1983) 2397

[Tow 87] I.S.Towner *Phys. Rep. 155* (1987) 264

[Wat+ 89] J.W.Watson *et al.*, *Phys. Rev. C40* (1989) 22

[Wil 84] B.H.Wildenthal, in *Progress in Particle and Nuclear Physics*, Vol.11, ed. by D.H.Wilkinson (Oxford: Pergamon Press) p.5

[Wil+ 87] A.Willis, M.Morlet, N.Marty, C.Djalali, G.M.Crawley, A.Galonsky, V.Rotberg and B.A.Brown, *Nucl. Phys. A464* (1987) 315

[Vet+ 89] M.C.Vetterli *et al.Phys. Rev. C40* (1989) 559